Chapter 4

Chapter 4

Design, Synthesis, and Biological Evaluation of Halogen-Substituted Novel α-Ketoamides as Potential Protein Aggregation Modulators

4.1. Introduction

The mounting prevalence of AD is increasingly alarming, given its profound neurological consequences. Afflicting the central nervous system, this multifaceted neurodegenerative disease compromises the cognitive abilities of over 20 million individuals worldwide, primarily seniors [1]. In the field of drug discovery, α-ketoamides stand out for their therapeutic versatility, benefiting conditions ranging from AIDS, Hepatitis C to AD [2]. Their recurrent presence in natural substances makes them invaluable assets for medicinal chemists aspiring to tailor compounds that mesh with diverse biological targets, thereby offering therapeutic avenues for myriad health challenges. Amongst the promising candidates for AD treatment, piperazine, and piperidine-based derivatives have stirred considerable interest [3, 4]. These organic entities, present in various drugs, are lauded for their multifaceted pharmacological effects. In AD's context, they promise enzyme inhibition, anti-amyloidogenic prowess, neuroprotection, and anti-inflammatory actions [5]. For instance, Donepezil, a piperidine derivative, reigns as a popular AD treatment, acting as an acetylcholinesterase (AChE) inhibitor [6]. Its piperidine scaffold also deters NMDA receptors, curbing aberrant neural activities and symptom exacerbation in AD sufferers. Similarly, piperazine derivatives are under scrutiny for their potential to impede Aβ aggregation and cytotoxicity, as evidenced by a recent study spotlighting certain piperazine compounds for their Aβ aggregation inhibition [7]. Another notable compound, aripiprazole, a quinolinone piperazine derivative categorized as an atypical antipsychotic, is speculated to alleviate AD's behavioral manifestations, though

its administration warrants caution due to potential adverse reactions [8].

In continuation to our efforts to explore α-ketoamides as potential protein aggregation modulators and motivated with the Aβ aggregation modulatory activity of **Compound 1** (**Chapter 3**), in this chapter, we explored halogen-substituted α-ketoamides as potential modulators of protein aggregation.

4.2. Objective

The objectives of this study are as follows:

- **Compound synthesis and characterization:** To synthesize different piperazine and piperidine substituted α-ketoamides and determine their structural properties through NMR spectroscopy and mass spectrometry.
- **In vitro Aβ aggregation assay:** To investigate the potential of synthesized α-ketoamide derivatives as Aβ aggregation modulators, assessing its inhibition of Aβ aggregation using ThT assay.
- **Physicochemical evaluation of hit compounds:** To ensure that the hit compounds meet the necessary physicochemical criteria for effective drug candidates, considering their solubility and BBB permeability as crucial factors in drug development.
- **In vitro heparin-induced tau aggregation assay:** To investigate the potential of α-ketoamides in preventing or reducing tau protein clumping triggered by heparin.
- **In vitro cytotoxicity assay:** To perform the in vitro cytotoxicity assay for the purpose of assessing the cytotoxic properties of specific hit molecules.
- **In vivo behavioral studies of the compound in Aβ-induced cognitive deficit mice model:** To evaluate the impact of the most potent hit compound on cognitive function in mice with Aβ -induced cognitive deficits.
- **In silico studies:** To perform molecular docking against Aβ peptide monomer and fibril structure as well as tau peptide followed by molecular dynamics simulation to evaluate

the binding mode of the compound with the target and to utilize DFT calculations to analyze the electronic structure, stability, and reactivity of the hit compound, including optimizing its stable structure and identifying reactive sites.

4.3. Results and Discussion

4.3.1. Chemistry

The starting materials (**2a-c**) were synthesized from compound (**1a-c**) by Wittig reaction in presence of Wittig salt and solvent THF. Then compounds (**2a-c)** underwent Sworn oxidation in the presence of DMSO and triphenylphosphine hydrobromide to produce β,γ-unsaturated-α-ketothioester (**3a-c**) [9], as illustrated in **Scheme 4.1**. Then β,γ-unsaturated α-ketoamides were synthesized from the β,γ-unsaturated thioester in presence of different substituted amines at room temperature [10].

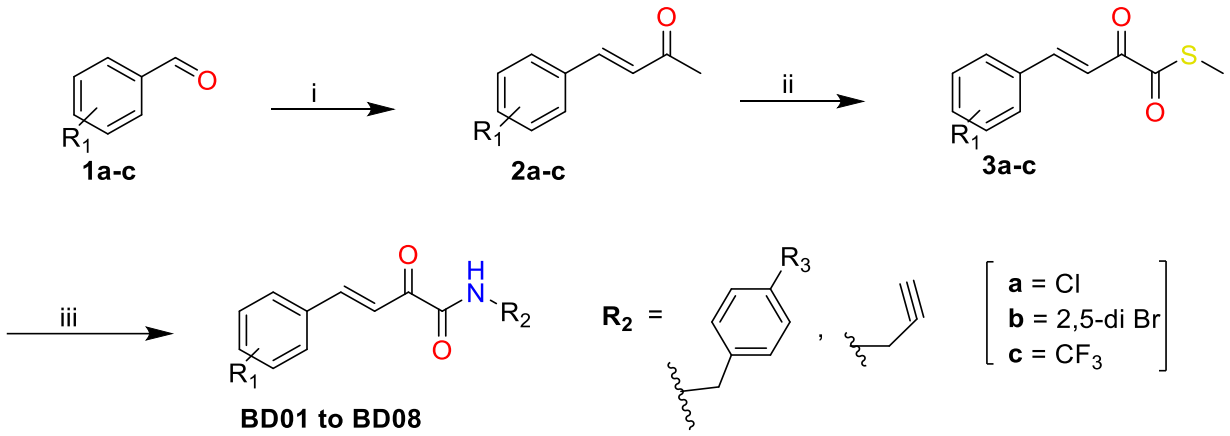

Scheme 4.1. Synthesis of novel β,γ- unsaturated α-ketoamides (BD01 to BD08). (i) Wittig salt (1-(Triphenylphosphoranylidene)-2-propanone), THF, 6-48 hrs, 90%; (ii) PPh_3.HBr, DMSO, 50 °C (iii) amines, DCM, rt.

The starting β,γ-unsaturated-α-hydroxy thioesters (**4a-c**) have been synthesized by the chemoselective reduction of β,γ-unsaturated α-ketothioesters (**3a-c**). Similarly, the β,γ-saturated-α-ketoamides (**5a-c**) are synthesized by the reaction of β,γ-unsaturated α-hydroxythioeter with different substituted piperazine and piperidine derivatives, illustrated in

Scheme 4.2.

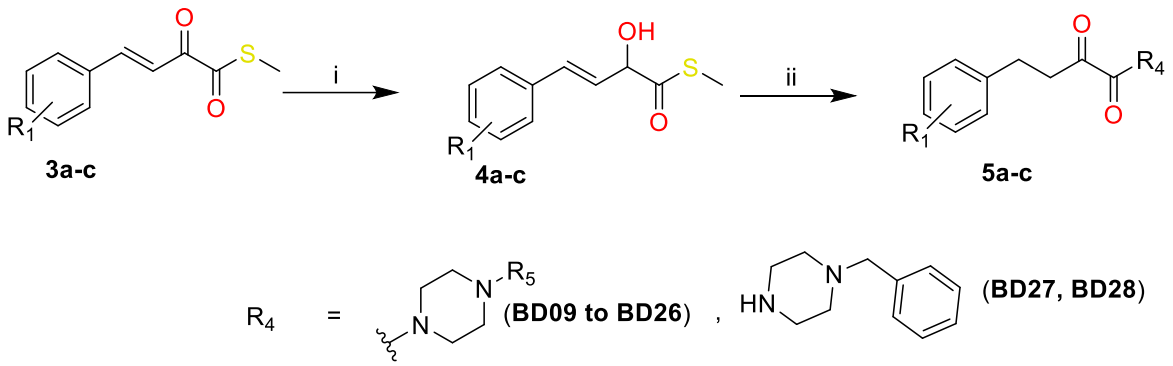

Scheme 4.2. Synthesis of novel β,γ-saturated-α-ketoamides (BD09 to BD28). (i) Et_3SiH, BF_3OEt_2, dry DCM, rt (ii) Amines, dry DCM, rt.

The synthesized β,γ-unsaturated α-hydroxythioesters has been used to successfully produce β,γ saturated α-ketoamides (**BD09** to **BD28**) without the need for metals or coupling agents. This process, facilitated by either primary or secondary amines, resulted in commendable to almost complete yields. Prior studies suggest that this reaction likely involves an amine-driven transformation of allylic alcohols, transitioning from Int-I to Int-II, leading to the production of the intended outcomes through amination (**Figure 4.1**).

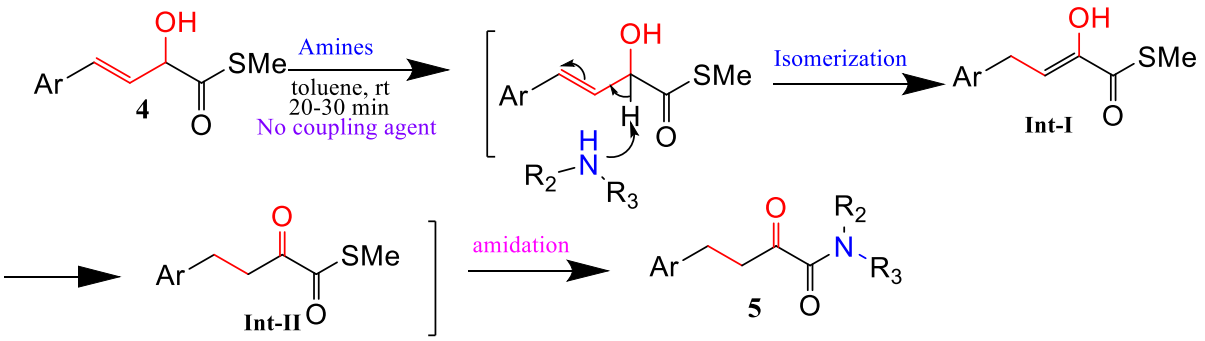

Figure 4.1. Plausible mechanism of the synthesis of β,γ-saturated α-ketoamides.

4.3.2. In Vitro Aβ Aggregation Assay and Structure Activity Relationship Study.

The synthesized compounds (**BD01-BD26**) were tested for their effect on the $A\beta_{42}$ aggregation using ThT assay. From the results of the Aβ aggregation assay, it was observed that many of

the compounds showed modulation of Aβ aggregation as indicated by the increase in the lag phase of the Aβ aggregation kinetics as shown in **Figure 4.2.**

Table 4.1. Structure of the synthesized β,γ-unsaturated α-ketoamides (BD01 to BD08).

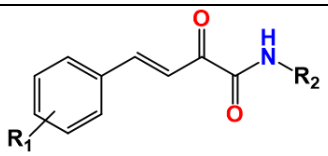

Compounds	R_1	R_2
BD01	4-Cl	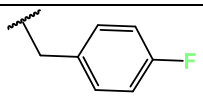
BD02	4-Cl	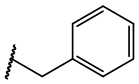
BD03	4-Cl	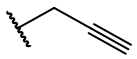
BD04	4-Cl	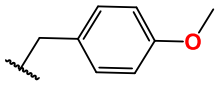
BD05	2,5-di Br	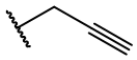
BD06	2,5-di Br	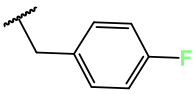
BD07	4-CF_3	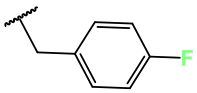
BD08	4-CF_3	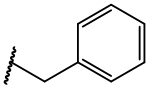

Table 4.2. Structure of the synthesized β, γ-saturated α-ketoamides (BD09 to BD28).

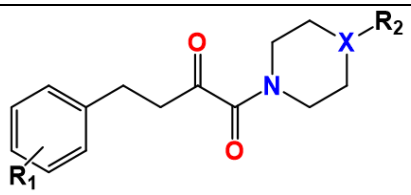

ID	R_1	X	R_2	ID	R_1	X	R_2
BD09	4-Cl	N	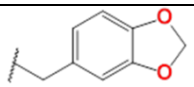	BD19	2,5-di Br	N	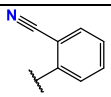
BD10	4-Cl	N	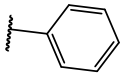	BD20	4-CF_3	N	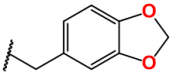
BD11	4-Cl	N	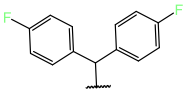	BD21	4-CF_3	N	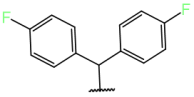
BD12	4-Cl	N	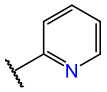	BD22	4-CF_3	N	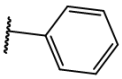
BD13	4-Cl	N	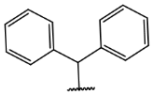	BD23	4-CF_3	N	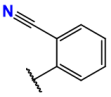
BD14	2,5-di Br	N	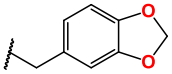	BD24	4-CF_3	N	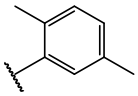
BD15	2,5-di Br	N	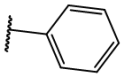	BD25	4-CF_3	N	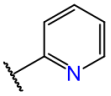
BD16	2,5-di Br	N	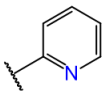	BD26	4-CF_3	N	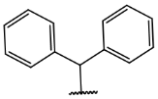
BD17	2,5-di Br	N	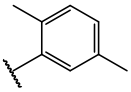	BD27	4-Cl	-	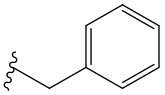
BD18	2,5-di Br	N	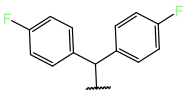	BD28	2,5-di Br	-	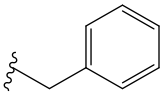

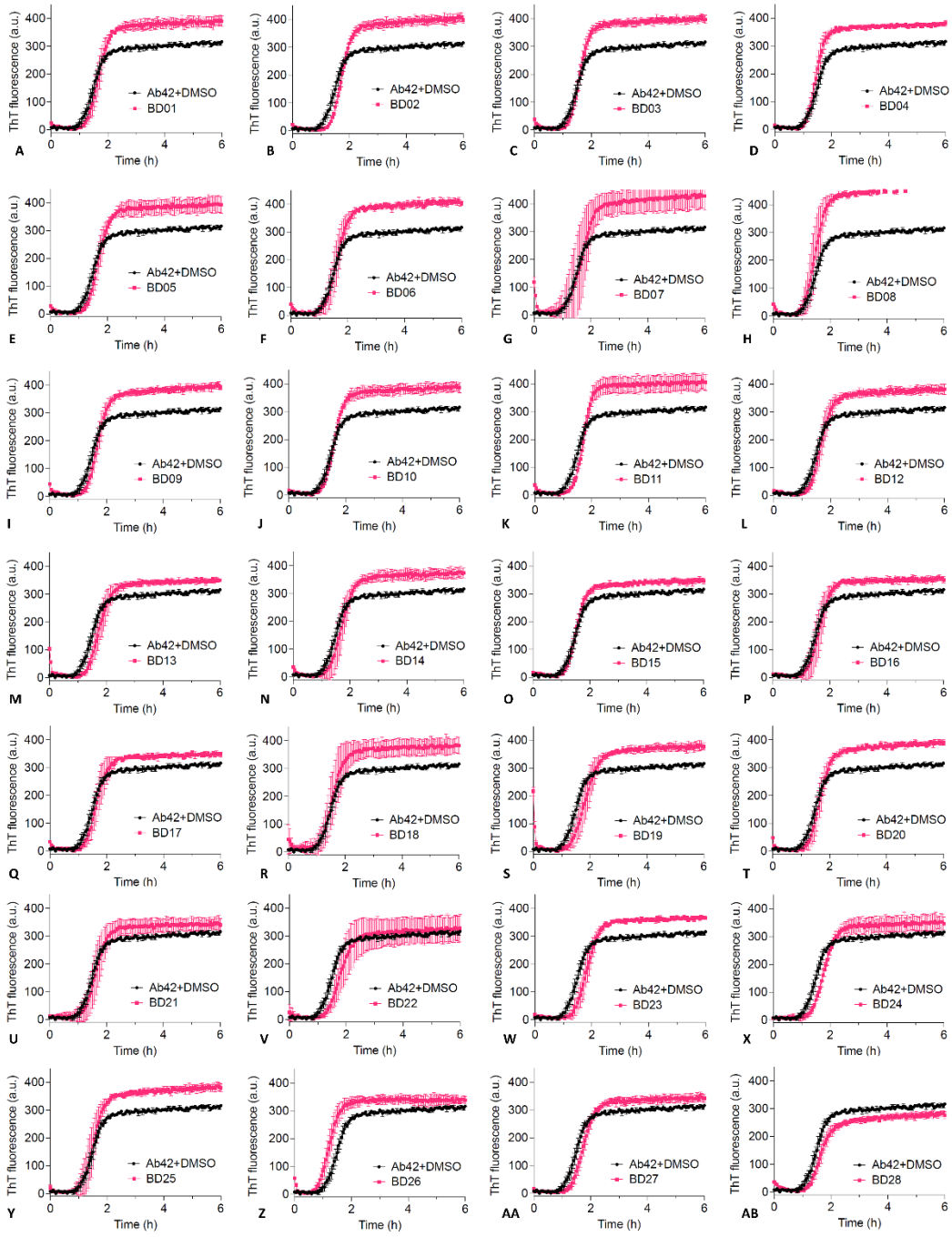

Figure 4.2. Aβ aggregation kinetics in the presence of compounds BD01-BD28. Figure 2A to 2AB represents the Aβ aggregation kinetics in the presence of 50 μM of the compound BD01 to BD28, respectively. The red graph indicates the ThT fluorescence of the compound well and the black graph represents the ThT fluorescence of the residual DMSO in reaction buffer equivalent to the amount of DMSO in the compound well.

Further to determine the modulation effect, the $\tau_{1/2}$ (aggregation half-time) for all the

compounds was calculated and compared with the control group ($A\beta_{42}$+ DMSO). Most of the compounds showed an increase in the $\tau_{1/2}$ while surprisingly compound BD23 showed a decrease in the $\tau_{1/2}$ indicating its pro-aggregation effect on the kinetics of Aβ aggregation. On the basis of the increase in the $\tau_{1/2}$, compounds BD19, BD23, BD24**,** and BD27 were selected as hit compounds and subjected to further evaluation. Compound BD22 also increased the $\tau_{1/2}$ considerably, however due to its variable effect in the triplicate readings (**Figure 4.3**), we didn't consider it as a hit compound.

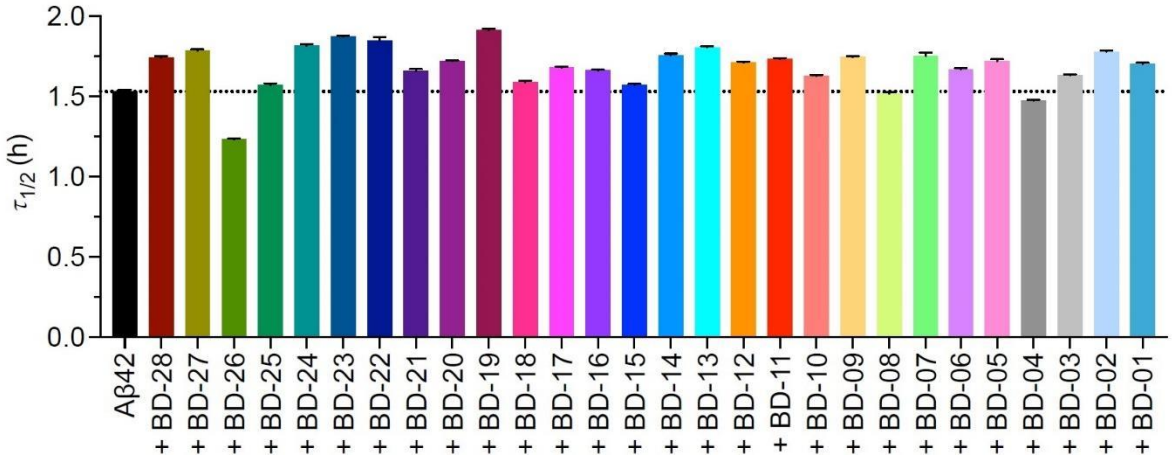

Figure 4.3. Aggregation half-time ($\tau_{1/2}$) of the compounds (BD01-BD28). The $\tau_{1/2}$ is determined by fitting the fibrillization traces of the $A\beta_{42}$ peptide with to a sigmoidal equation given by Eq. ($F=F0+A/(1+\exp[rmax\ (\tau 1/2-t)]$) where *A* is the amplitude and F_0 is the base value.

Moreover, based on the effect of compounds on the Aβ aggregation, a Structure-Activity Relationship (SAR) is derived for these piperazine-based compounds (**BD01-BD28**). The overall SAR is presented in **Figure 4.4**. Notably, halogen substitution at positions R_1 and R_3 on ring A plays a pivotal role in determining the activity of the compounds. Introduction of a trifluoromethyl group at the R_2 position enhances the potency compared to when a chlorine group is present. Moreover, substituting the piperazine moiety with a benzyl piperidine group marginally augments the compound's potency. Conversely, the replacement of R_4 on ring B

with a 2,5-methyl phenyl group diminishes potency relative to the nitrile-substituted group. The incorporation of a nitrile-substituted phenyl group at the R_4 position has been observed to elevate potency.

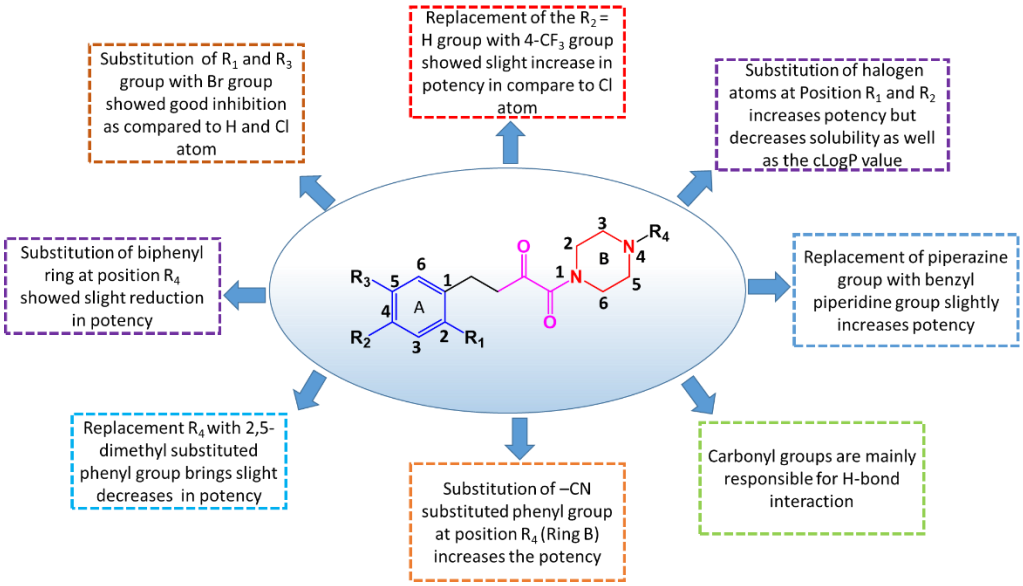

Figure 4.4. Structural Activity Relationship (SAR) study of compounds (BD01-BD28) based upon their effect on Aβ aggregation kinetics.

4.3.3. Solubility Study of the Hit Compounds

The solubility of drug candidates plays a pivotal role, especially when targeting treatments for conditions such as AD. It ensures effective administration and absorption within the body. It has been observed that many potent lead compounds do not progress to clinical trial stages due to their reduced bioavailability, which is often a consequence of inadequate solubility [11, 12]. This underscores solubility as a fundamental consideration during the initial stages of drug discovery. Poorly soluble molecules present challenges during in vitro and in vivo evaluations and can complicate the drug development process [11]. Hence, for drugs aimed at targeting the brain, achieving an optimal balance between solubility and lipophilicity is vital to enhance their efficacy. In our study, we assessed the solubility of hit compounds BD19, BD23, BD24, and BD-27. The solubility data for these compounds is presented in **Table 4.3**. Solubility of four

hit compounds are ranging from 0.037 to 0.041 mg/mL.

Table 4.3. Kinetic solubility study of hit compounds BD19, BD23, BD24 and BD27.

Compounds	**Kinetic solubility (mg/mL) Mean ± SD (N=3)**	**cLogP***
BD19	0.041 ± 0.0012	5.09
BD23	0.045 ± 0.0012	4.25
BD24	0.038 ± 0.0018	5.42
BD27	0037 ± 0.0033	5.17

* LogP calculated using RDKit tool

4.3.4. In Vitro Blood Brain Barrier Permeability Study of the Compound BD23.

The BBB permeability is one of the crucial factors for all CNS-acting drugs and thus we determined the BBB permeability of compounds BD23 which emerged as soluble in the solubility assay. The BBB permeability was estimated using the Parallel Artificial Membrane Permeation Assay (PAMPA) BBB model. Compound BD23 showed an effective permeability (P_e) of 10.66 ± 8.11 $\times 10^{-6}$ cm s^{-1} which placed it in the BBB permeable category (**Table 4.4**). For comparison, two positive controls (BBB permeable drugs) and one negative control (BBB impermeable drug) were used in the assay.

Table 4.4. PAMPA-BBB permeability of the compound BD23 (PC: Positive Control, NC: Negative Control).

Compound	**Permeability Rate (Pe) ($\times 10^{-6}$ cm s^{-1}) Mean ± SD (N=2)**
BD23	10.66 ± 8.11
Promazine Hydrochloride (PC)	6.83 ± 0.82
Diclofenac (NC)	3.32 ± 0.48
Donepezil (PC)	13.8 ± 13.7

4.3.5. Compound BD23 Inhibited Heparin-induced Tau Aggregation.

The compound BD23 emerged as a potential lead compound owing to its effect on the Aβ aggregation kinetics, moderate solubility and good BBB permeability. Thus, we further explored its effect on the tau aggregation using heparin-induced tau aggregation assay. The results indicated that compound BD23 inhibited the tau aggregation more than fifty percent as compared to the control (**Figure 4.5**) at 100 µM concentration. Surprisingly, at 200 µM concentration, BD23 inhibited tau aggregation by around thirty percent however, it was not statistically significant as compared to the control which might be due to the large variation in the samples or the low solubility of compound BD23 which on addition to the buffer might get precipitated at higher concentration.

Figure 4.5. Effect of compound BD23 on tau aggregation monitored by ThT after 72 hrs. incubation at 37 °C. The # represents significance compared to the BD23 untreated control group (tau + heparin). Data were expressed as Mean ± SD and analyzed by one-way ANOVA (Tukey's multiple comparisons test) (n=2). ***p<0.001, **p<0.01, *p<0.05. ns = non-significant p value.

4.3.6. In Vitro Cytotoxicity Assay

The effect of compounds BD11, BD19, BD20, BD22, BD23, BD24 and BD27 on SH-SY5Y neuroblastoma cell line was evaluated to test their cytotoxicity using MTT assay. All the tested

compounds except BD11 and BD19 showed no significant cytotoxicity while compound BD11 showed around fifty percent cell viability after 24 hrs of treatment with a 50 µM concentration and surprisingly, compound BD19 showed increased metabolic activity of the cells in the assay (**Figure 4.6**). Microscopic images also showed no major changes in the cell morphology for the compounds treated well except BD11 treated cells (**Figure 4.7**).

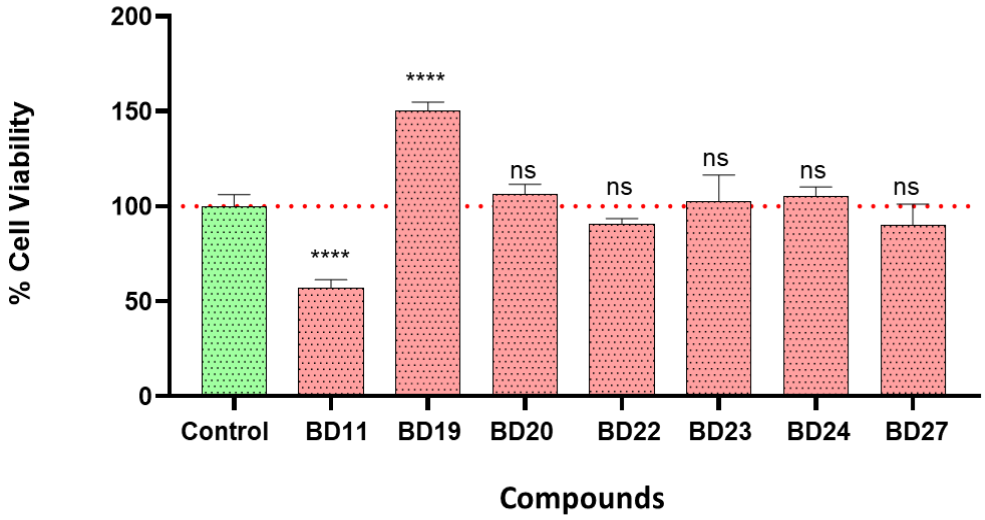

Figure 4.6. **Histograms of the viability of SH-SY5Y cells upon the treatment with different compounds at 50 µM concentrations for 24 hrs.** Data were expressed as Mean ± SD and analyzed by one-way ANOVA (Tukey's multiple comparisons) (n=6). **** represents significance compared to the control group ($p<0.0001$), ns- not significant.

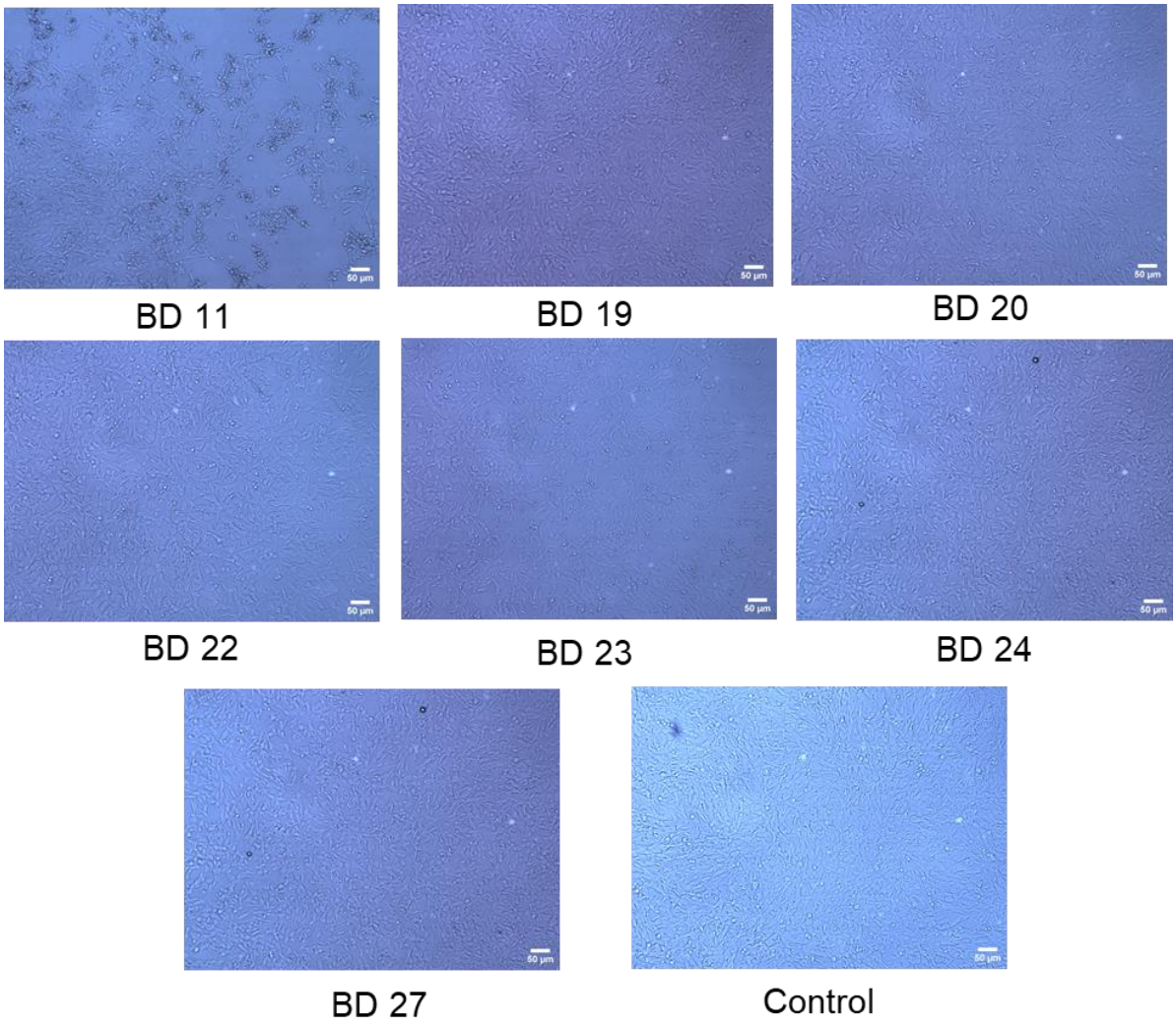

Figure 4.7: **Morphological changes in SHSY-5Y cells were observed under an inverted light microscope (10× magnification).** The scale bar is 50 µM.

4.3.7. In Vivo Behavioral Studies of Compound BD23 in Aβ-induced Cognitive Deficit Mice Model.

4.3.7.1. BD23 improved the learning & and memory impairment in Aβ injected mice in Elevated Plus Maze test

The Elevated Plus Maze (EPM) test is a prominent behavioral tool utilized in neuroscience and psychological research for the quantification of anxiety-related behaviors in rodent models, primarily mice and rats. The test is predicated on the intrinsic aversion these animals exhibit towards elevated platforms and open expanses. The term "transfer latency" is typically

employed to describe the duration required for an animal to transition from one designated region or state to another. **Figure 4.8A** and **4.8B** depict a notable observation: the healthy control group exhibited a diminished percentage of retention transfer latency in comparison to the disease control group, which demonstrated a higher percentage of initial retention transfer latency. The cohorts treated with the compound BD23, administered at dosages of 1 mg/kg and 2 mg/kg body weight, did not show statistically significant effects, with the observed initial transfer latencies being approximately 70% and 60%, respectively. In contrast, the cohort administered a dosage of 5 mg/kg body weight demonstrated a pronounced reduction in initial transfer latency, approximately 24%. This indicates that, at this particular dosage, the compound BD23 may have therapeutic potential, augmenting cognitive function in Aβ-injected mice.

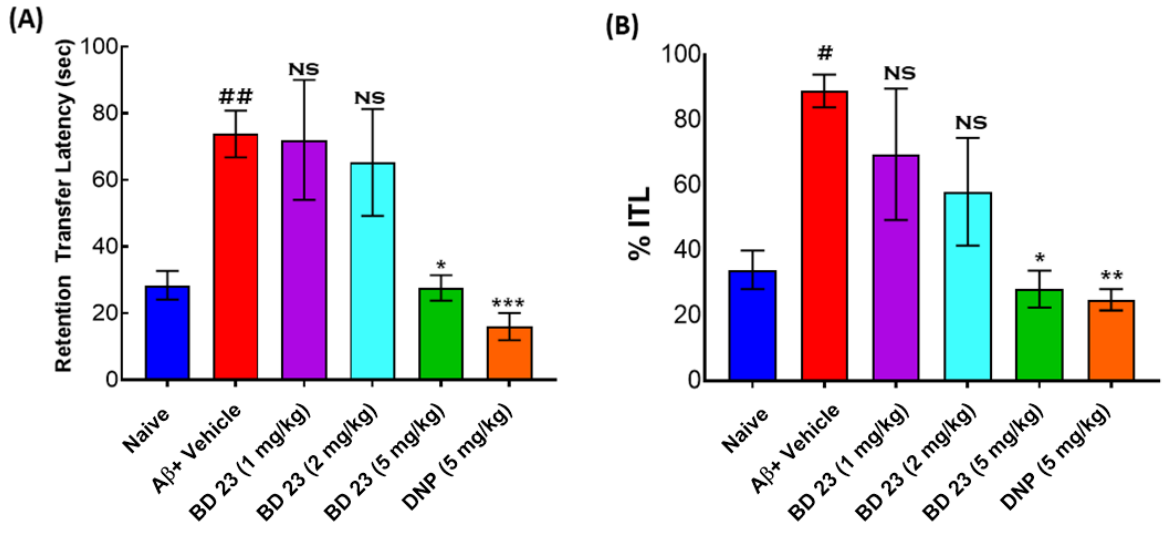

Figure 4.8. Effect of BD23 on Retention Transfer Latency and % Initial Transfer Latency (% ITL). Retention Transfer Latency (**A**), % Initial Transfer Latency (**B**). Data were expressed as Mean ± SEM and analyzed by one-way ANOVA (Bonferroni's & Tukey's multiple comparisons) (n=5). # represents significance compared to the control group ($p<0.05$), * ($p<0.05$), ** ($p<0.01$) represents significance compared to the vehicle group. BD23 doses (1, 2 & 5 mg/kg i.p), Donepezil (DNP- 5 mg/kg i.p)

4.3.7.2. BD23 increased the discrimination ratio in Aβ injected mice in a novel object Recognition test

The Novel Object Recognition (NOR) test is a commonly used behavioral assay to evaluate recognition memory in animals, especially rodents. The premise is based on the animal's natural curiosity; animals will typically spend more time exploring a novel object compared to a familiar one if they remember the familiar object [13]. The main measure of interest is the relative time the animal spends exploring the novel object compared to the familiar one. If the animal spends more time with the novel object, it suggests that it remembers the familiar one, indicating a working recognition memory. If it does not show a preference, it may indicate memory impairment. In a comparative analysis of cognitive abilities pertaining to novel object recognition, the standard cohort exhibited a 57 % inclination, suggestive of heightened curiosity towards the unfamiliar object. When we compare the Naive group with Aβ treated group, showed a significant reduction in the discrimination index. The group treated with 1 mg/kg, 2 mg/kg of dose showed no improvement in cognitive functions but the group treated with 5 mg/ kg of dose showed a significant effect in improving recognition memory in Aβ injected mice.

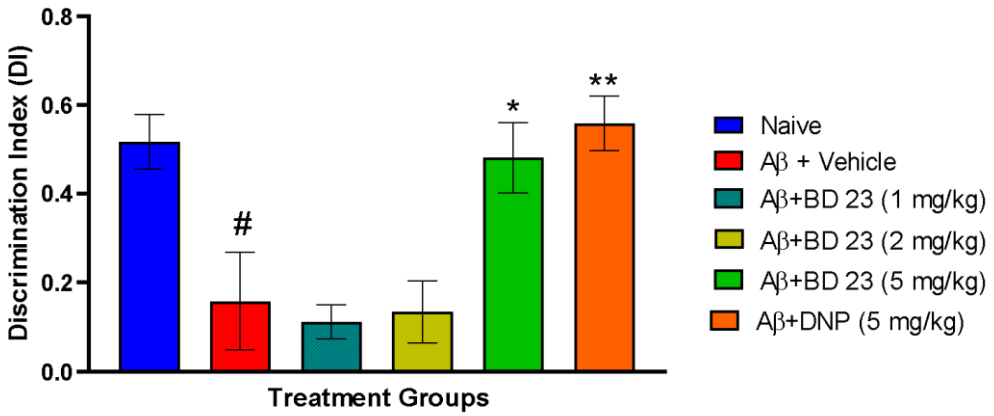

Figure 4.9: Effect of BD23 on Discrimination Ratio in Novel Object Recognition Test. BD23 administration in $A\beta_{25-35}$ injected mice significantly improved the discrimination index. Data were expressed as Mean ± SEM and analyzed by one-way ANOVA (Tukey's multiple

comparisons) (n=5). # represents significance compared to the control group ($p<0.05$), * ($p<0.05$),** ($p<0.01$) represents significance compared to the vehicle group. BD23 doses (1, 2 & 5 mg/kg i.p), donepezil (DNP- 5 mg/kg i.p)

Conversely, the control group that received an injection of $A\beta_{25-35}$ demonstrated a notably diminished cognitive ability, recording only 43 %. When subjected to the compound BD23 at a dosage of 1 mg/kg, the cognitive ability was measured at 45 %. Interestingly, an increased dosage of BD23 to 2 mg/kg manifested a pronounced decline in curiosity towards the new object. Nevertheless, when the dosage was increased to 5 mg/kg, there was a significant enhancement in the inclination towards novel object exploration.

4.3.7.3. BD23 did not affect motor coordination in Aβ injected mice in Rotarod test

The Rotarod test is a commonly used method in neurobiology to assess motor coordination and balance in rodents, primarily mice and rats. The test involves placing the animal on a rotating rod and measuring how long it can stay on the rod without falling [14]. All three groups disease control group, compound treated group and Donepezil treated group did not show any significant difference suggesting that compound BD23 didn't show any effect on motor coordination in mice (**Figure 4.10)**.

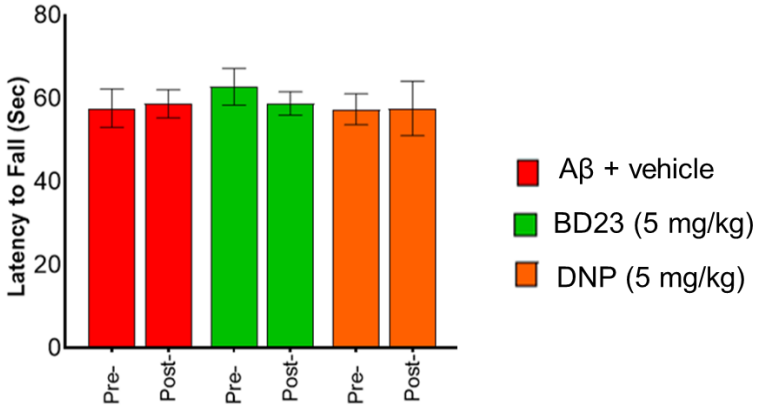

Figure 4.10. BD23 did not affect motor coordination in $A\beta_{25-35}$ injected mice. BD23 administration in $A\beta_{25-35}$ injected mice showed no sign of motor incoordination in the rotarod

test. Data were expressed as Mean ± SEM and analyzed by one-way ANOVA (Tukey's multiple comparisons) (n=5). # represents significance compared to the control group ($p<0.05$), * ($p<0.05$),** ($p<0.01$) represents significance compared to the vehicle group. BD23 doses (1, 2 & 5mg/kg i.p), Donepezil (DNP- 5 mg/kg i.p)

4.3.8. In Silico Molecular Docking Study

To investigate the molecular interactions of the synthesized compounds (BD01-BD28), we performed molecular docking study using Deep Learning algorithm based docking program, Gnina [15] against Aβ monomer (PDB ID:1IYT), Aβ fibril (PDB:2BEG) and tau monomer [16]. Since tau is an intrinsically disordered protein, we performed Replica Exchange Molecular Dynamics (REMD) simulation to obtain representative tau monomer 3D structures (Cluster 6 and Cluster 8) and used them for molecular docking study. The details of REMD simulation is discussed in **Chapter 6, Section 6.3.2.** The molecular docking scores of the compounds are given in **Table 4.5** and the molecular interactions of BD19, BD23, BD24, and BD27 are discussed in the following sections.

4.3.8.1. Molecular Docking of the hit compounds against Aβ monomer structure (1IYT)

The docking interactions in the form of 3D and 2D interaction diagrams is shown in **Figure 4.11**. The compound BD19 interacted with Aβ monomer through hydrophobic interactions with LEU17, PHE20, ALA21, VAL24, ILE31, LEU34, and MET35 amino acid residues (**Figure 4.11A**). Compound BD23 showed hydrophobic interactions with VAL12 and PHE12 residues (**Figure 4.11B**). The compound BD24 interacted with Aβ monomer through hydrophobic interactions with VAL36, LEU34, ILE31 and PHE20, VAL24 (**Figure 4.11C**). The compound BD27 showed hydrophobic interactions with residues LEU17, VAL18, ALA21 **(Figure 4.11D**).

Table 4.5. Molecular docking score of the compounds (BD01-BD28) against Aβ monomer (PDB ID:1IYT), Aβ fibril (PDB:2BEG) and tau monomers (Cluster 6 and Cluster 8).

Compound	1IYT			2BEG			Cluster 6			Cluster 8		
	Affinity (Kcal/mol)	CNN Score	CNN Affinity	Affinity (Kcal/mol)	CNN Score	CNN Affinity	Affinity (Kcal/mol)	CNN Score	CNN Affinity	Affinity (Kcal/mol)	CNN Score	CNN Affinity
BD01	-4.105	0.733	4.001	-6.214	0.747	5.089	-5.053	0.568	4.015	-6.183	0.643	4.167
BD02	-5.362	0.704	4.003	-4.699	0.773	5.664	-4.454	0.543	3.995	-4.727	0.613	4.022
BD03	-3.551	0.82	3.831	-5.88	0.776	4.87	-6.17	0.606	4.333	-6.456	0.662	4.146
BD04	-4.431	0.735	4.106	-4.854	0.732	5.508	-4.877	0.467	4.377	-6.235	0.632	4.602
BD05	-3.394	0.735	4.002	-5.691	0.736	5.161	-5.609	0.527	4.86	-6.006	0.568	3.978
BD06	-4.184	0.705	4.452	-6.939	0.636	5.503	-4.72	0.612	4.643	-6.334	0.555	4.482
BD07	-4.474	0.726	4.173	-5.156	0.705	5.809	-5.274	0.606	3.795	-5.655	0.535	4.335
BD08	-5.809	0.754	4.292	-5.136	0.657	5.118	-5.173	0.543	4.05	-5.093	0.638	4.149
BD09	-4.647	0.629	4.166	-5.123	0.522	4.852	-6.507	0.533	4.982	-5.85	0.381	4.498
BD10	-4.301	0.677	4.372	-6.13	0.724	5.352	-5.614	0.393	4.39	-6.41	0.484	4.605
BD11	-4.359	0.743	5.064	-5.952	0.577	6.542	-6.845	0.365	5.143	-7.516	0.281	4.994
BD12	-3.672	0.547	4.288	-6.068	0.691	5.815	-4.661	0.428	3.982	-7.645	0.498	5.441
BD13	-4.58	0.495	4.769	-7.102	0.531	5.986	-5.572	0.354	4.528	-5.425	0.393	4.667
BD14	-5.787	0.489	4.511	-6.162	0.456	5.859	-5.152	0.322	4.45	-6.784	0.346	4.964
BD15	-4.194	0.65	4.743	-6.628	0.741	5.643	-5.85	0.31	4.39	-5.577	0.343	4.777
BD16	-3.925	0.615	4.291	-6.319	0.697	5.913	-4.954	0.434	4.836	-8.171	0.379	5.765
BD17	-4.463	0.452	4.851	-5.281	0.571	6.112	-5.584	0.366	4.673	-5.513	0.287	4.625
BD18	-4.556	0.453	5.144	-5.552	0.492	5.695	-5.975	0.239	5.051	-8.02	0.236	5.155
BD19	-4.211	0.474	4.808	-6.383	0.686	5.864	-5.255	0.434	4.732	-4.695	0.372	4.951
BD20	-4.709	0.552	4.504	-5.604	0.463	5.837	-5.765	0.389	4.473	-6.842	0.338	4.695
BD21	-4.669	0.379	5.258	-6.121	0.594	6.693	-5.562	0.456	5.074	-5.394	0.343	4.933
BD22	-4.553	0.714	4.431	-5.505	0.749	5.841	-4.797	0.561	3.984	-5.267	0.512	4.422
BD23	-4.194	0.688	4.746	-6.731	0.571	5.489	-4.937	0.444s	4.478	-5.001	0.493	4.658
BD24	-4.711	0.648	4.773	-5.486	0.616	6.064	-5.635	0.394	4.882	-6.676	0.355	4.897
BD25	-3.914	0.534	4.334	-5.437	0.631	5.7	-4.9	0.473	4.432	-5.046	0.467	4.484
BD26	-4.532	0.714	4.809	-7.088	0.468	5.876	-5.832	0.217	4.691	-5.225	0.45	4.918
BD27	-3.715	0.667	4.734	-5.656	0.857	6.333	-6.844	0.419	4.985	-6.842	0.507	4.839
BD28	-4.525	0.739	5.037	-5.722	0.657	5.432	-6.572	0.311	5.577	-5.994	0.436	5

CNN Score : convolutional neural networks score, CNN Affinity : convolutional neural networks affinity.

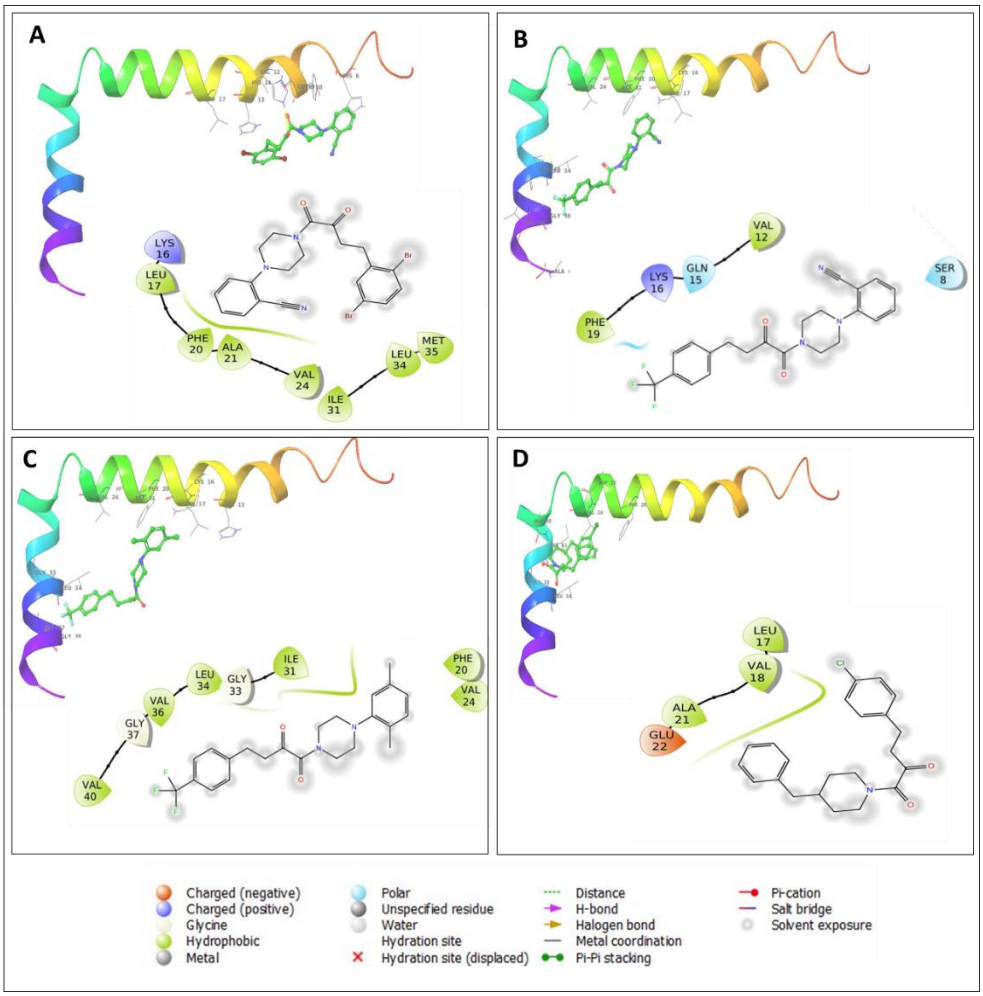

Figure 4.11. The 3D and 2D interaction images of compounds BD19 (A), BD23(B), BD24 (C) and BD27 (D) with Aβ-monomer (1IYT).

4.3.8.2. Molecular Docking of the hit compounds against Aβ fibril structure (2BEG)

The docking interactions in the form of 3D and 2D interaction diagrams is shown in **Figure 4.12**. The 2,5-dibromo phenyl group of compound BD19 showed hydrophobic interactions with residues VAL_B36, LEU_B34, ILE_B32, VAL_A36, LEU_A34, ILE_A32. (**Figure 4.12 A**).

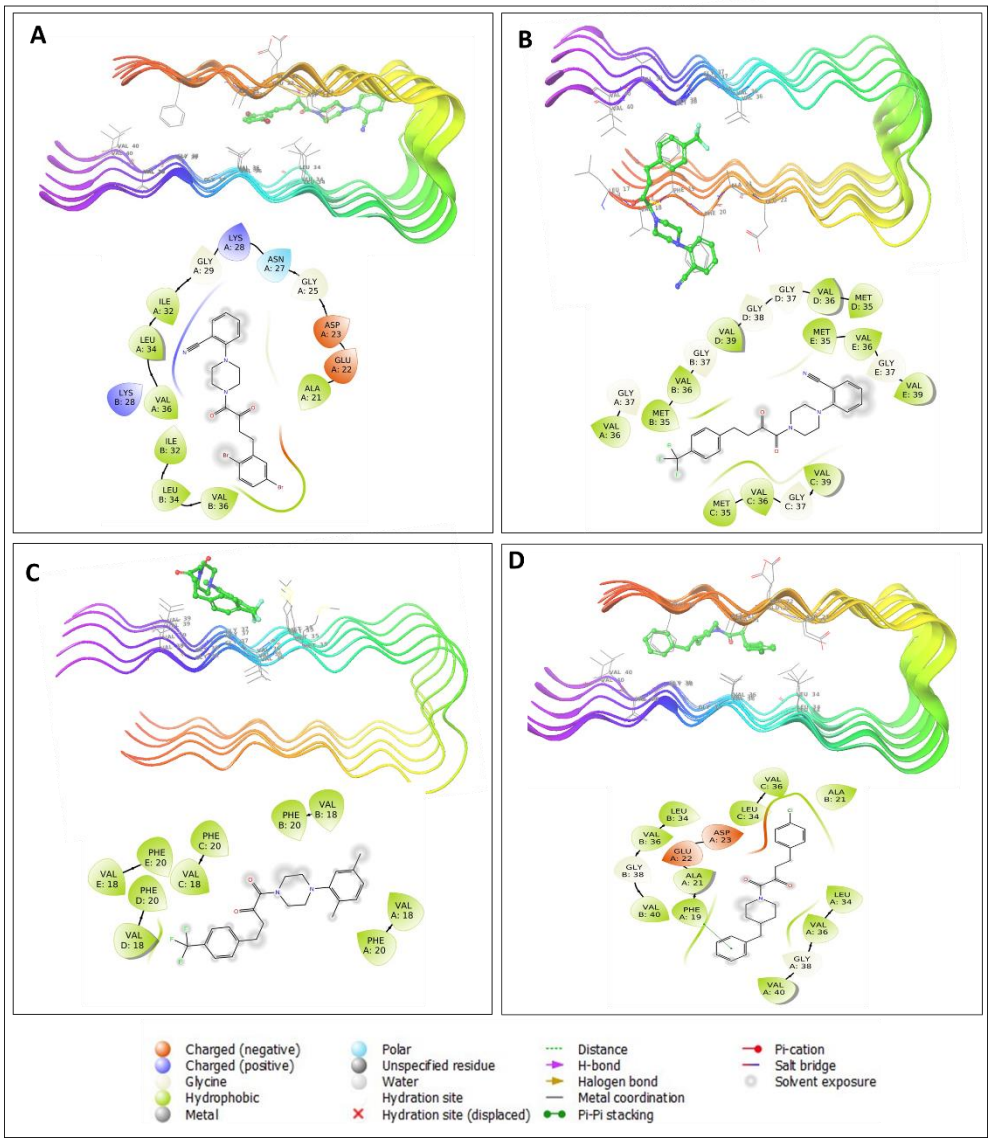

Figure 4.12. The 3D and 2D interaction images of compounds BD19 (A), BD23 (B), BD24 (C) and BD27 (D) with Aβ-pentamer (2BEG).

The trifluromethyl group and α-ketoamide group of BD23 is encased in the hydrophobic pocket formed by the residues and MET_B35, VAL_C36, VAL_C39, MET_C35, VAL_B36, VALD39, MET_E35, VAL_E36, and VAL_E39 (**Figure 4.12B**). The 3D and 2D interaction of compound BD24 showed that the compound is encased in the hydrophobic pocket formed by the residues VAL_A18, PHE_A20, VAL_B18, PHE_B20, PHE_C20, VAL_C18, VAL_D18, PHE_D20, PHE_E20, VAL_E18 residues (**Figure 4.12C)**. The molecular docking of compound BD27 revealed that the 4-chloophenyl and benzyl piperazine group undergoes

hydrophobic interactions with ALA_B21, VAL_C36, LEU_C34, and ALA_21, VAL_A44, PHE_A19 residues respectively (**Figure 4.12D)**.

4.3.8.3. Molecular Docking of the hit compounds against tau monomer structure (Cluster 06)

The docking interactions in the form of 3D and 2D interaction diagrams is shown in **Figure 4.13**. The molecular docking study of compound BD19 revealed that the compound undergoes hydrophobic interactions with VAL337, PRO364 and ILE308 residues (**Figure 4.13A**). The molecular docking study of BD23 revealed that the compound showed hydrophobic interactions with the residues like ILE308, VAL309, PRO364, ILE308, TYR310, VAL313. The π-electrons of the CN substituted phenyl group undergoes π-cation interaction with LYS294 and the nitrogen atom of CN group showed hydrogen bond interaction with LYS298 (**Figure 4.13B)**. The molecular docking study of compound BD24 revealed that the compound showed hydrophobic interactions with the residues like VAL306, ILE308, PRO364, VAL363, ILE360 (**Figure 4.13C)**. The 3D and 2D interactions of compound BD27 showed that 4-chlorophenyl group undergoes hydrophobic interaction with VAL300, PRO301, VAL309. The carbonyl oxygen atom of α-ketoamide group showed hydrogen bond interaction with SER324 residue (**Figure 4.13D**).

4.3.8.4. Molecular Docking of the hit compounds against tau monomer structure (Cluster08)

The docking interactions in the form of 3D and 2D interaction diagrams is shown in **Figure 4.14**. The molecular docking of compound BD19 with cluster 08 showed that the cyano phenyl piperazine group and 2,5-dibromo phenyl group are encased in the hydrophobic pocket formed by the residues PRO301, VAL300, PRO364, VAL363, CYS291, VAL306, ILE308, VAL309, TYR310. (**Figure 4.14A**).

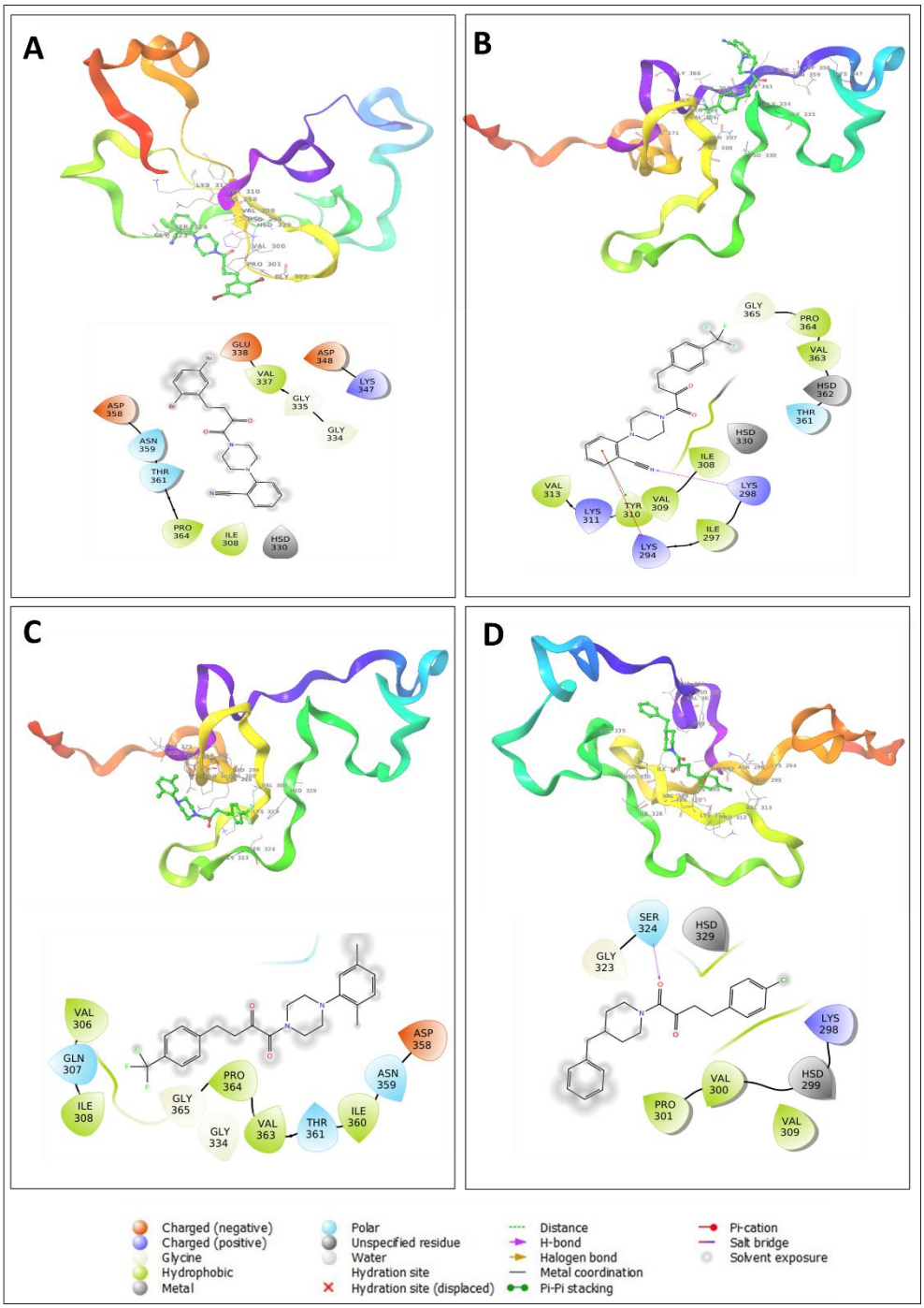

Figure 4.13. The 3D and 2D interaction images of compounds BD19 (A), BD23 (B), BD24 (C), and BD27 (D) tau monomer cluster 6 (C06).

The molecular docking of compound BD23 with cluster 08 revealed that the 4-trifluromethyl phenyl and cynophenyl piperazine group showed hydrophobic interaction with ILE360, VAL363, PRO364, TYR310, VAL309, ILE308, VAL306, ILE297, and CYS291 (**Figure**

4.14B).

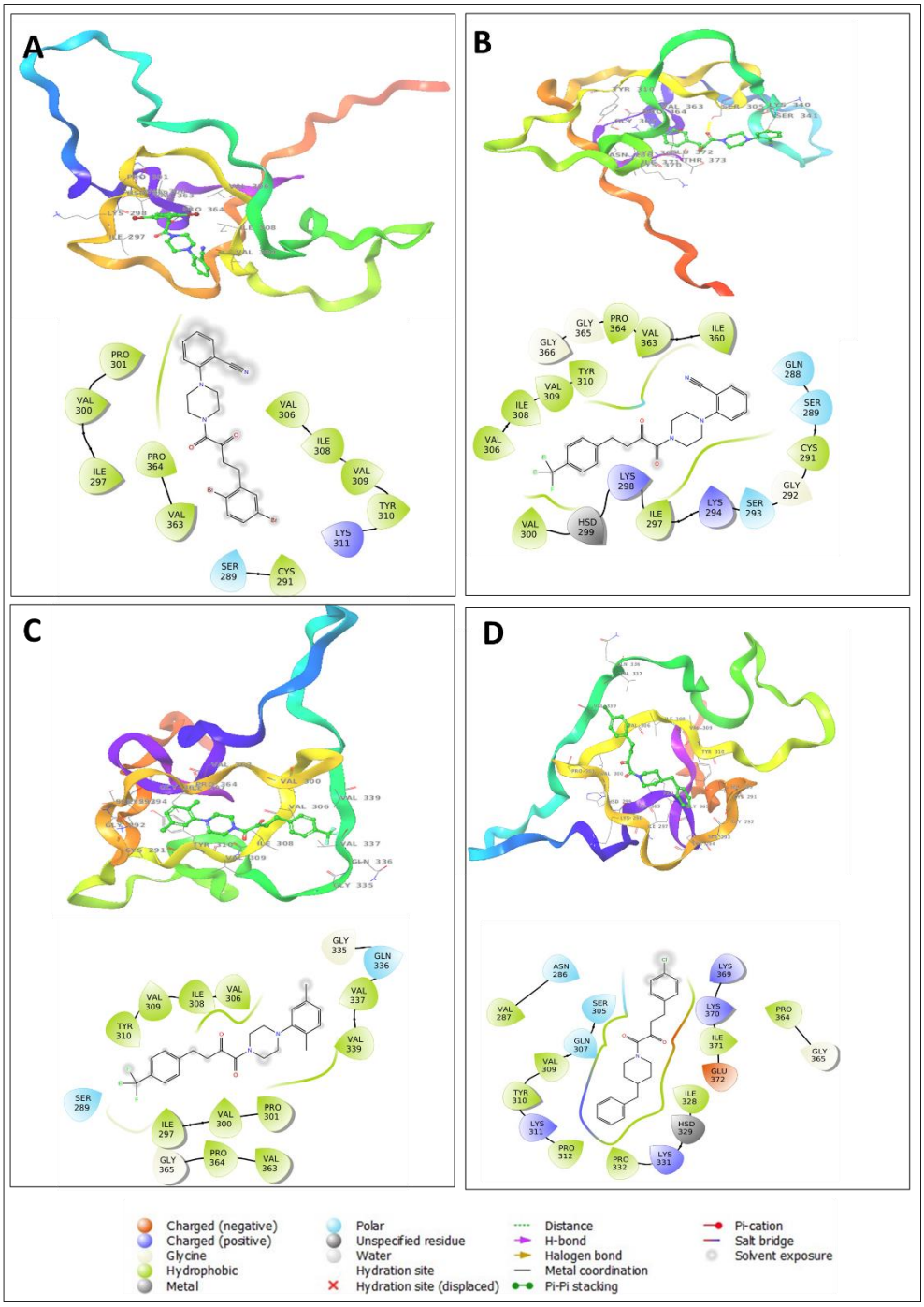

Figure 4.14. The 3D and 2D interaction images of compounds BD19 (A), BD23 (B), BD24 (C) and BD27 (D) against tau monomer cluster 8 (C08).

The molecular docking of compound BD24 with tau monomer (C08) showed that the molecule is encased in the hydrophobic pocket formed by the residues VAL337, VAL339, VAL337,

VAL306, ILE308, TYR310, VAL300, ILE297, VAL363, PRO364 (**Figure 4.14C**). The 3D and 2D interaction of the compound BD27 revealed that the compound showed hydrophobic interactions with PRO364, ILE371, ILE328, VAL309, TYR310, and VAL287 residues (**Figure 4.14D**).

4.3.9. In silico Quantum Chemical Studies

4.3.9.1. Geometry optimization of lead compound BD23 using Density Functional Theory

DFT study of compound BD23 was performed using energy model and basis set B3LYP/6-311G (d, p) and we found that a total number of fifty atoms are involved in the structure of compound BD23. The bond angle and bond lengths were calculated. The optimized structure from DFT is represented in the **Figure 4.15**.

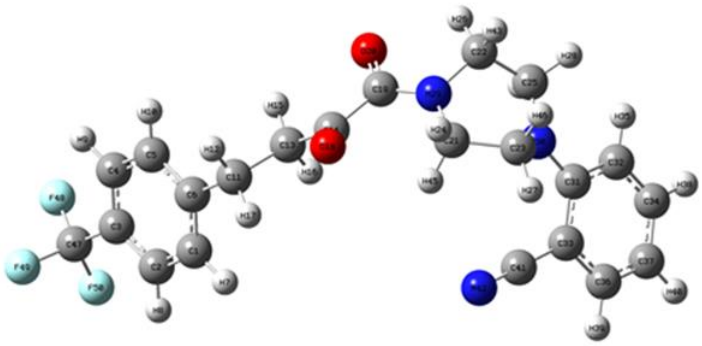

Figure 4.15. Optimized structure obtained from DFT study of BD23.

4.3.9.2. Molecular Electrostatic Potential

MEP is a property derived from DFT calculations that provides information about the electrostatic potential distribution around a molecule. It helps in understanding the reactivity and chemical properties of a molecule. The MEP is commonly visualized as a color-coded map, where regions of high electron density are represented by red or yellow colors, indicating negative values of the potential, while regions of low electron density are represented by blue colors, indicating positive values of the potential. The MEP provides information about the

sites of nucleophilic and electrophilic reactivity in a molecule. The areas with pronounced negative potential within the molecule were pinpointed. In MEP map, the O30, O19, and N8 group atoms are encircled by red indicators, signaling electrophilic activity. Conversely, the vicinity near N12 and the area close to the carbon atoms suggest nucleophilic behavior, as highlighted by the blue hue in the MEP map. The overall electron density map of compound BD23 shown in **Figure 4.16**.

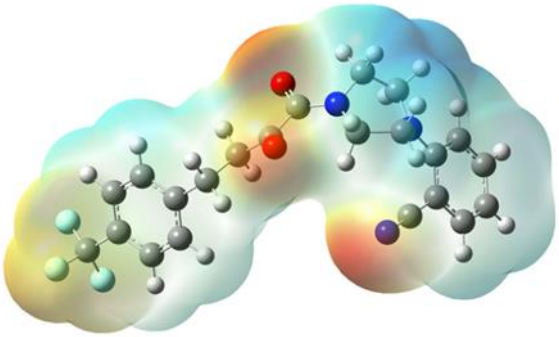

Figure 4.16. Molecular Electrostatic Potential map of compound BD23.

4.3.9.3. Frontier Molecular Orbitals (FMOs)

The **Figure 4.17** shows the HOMO-LUMO diagram of compound BD23 and the compound appears to be more reactive (E= EHOMO-ELUMO =0.1435 eV) based on the data obtained.

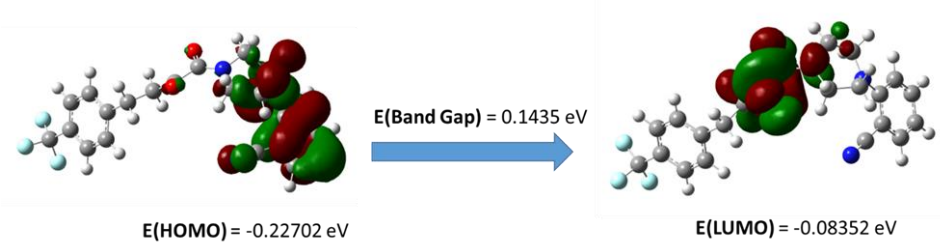

Figure 4.17. HOMO and LUMO diagrams of compound BD23.

4.3.10. Molecular Dynamics Simulation Study

To investigate the stability of the docked complex, the lead compound BD23 in complex with Aβ monomer, fibril and tau monomer clusters 6 and 8 were subjected to a 200 ns molecular dynamics simulation.

4.3.10.1. Molecular Dynamics Simulation of the BD23-Aβ monomer (1IYT) complex

The MD study has been performed in order to evaluate the dynamic behavior of the compound BD23-Aβ monomer complex. The radius of gyration (RoG) is a metric used in MD that aids to measure the distribution of the atoms of the protein around the three dimensional space. The RoG value quantifies how much the atoms are spread out from the center of the mass of molecule. Thus, providing us with an insight into the overall size and compactness of the biomolecules, enabling us to study the structural transitions, protein folding, aggregation, and other conformational changes that might occur during the MD simulation. RoG value of the complex BD23 with Aβ (1IYT) is depicted in (**Figure 4.18A**). A relatively high but stable RoG value within the range of 1-1.5 nm was observed that explains that the system is relatively flexible and is constantly changing its quaternary geometrical dimensions. The system seems to stabilize more around 100 ns time frame after which the RoG value is stable at 1nm. Thus, no indication of abrupt motions during the simulation time period of 200 ns were observed. Furthermore, the root mean square deviation (RMSD) of the simulated system was evaluated (**Figure 4.18B**) for the overall stability of the simulated system, as it measures the difference between the backbone of the protein from its initial position at the starting of the simulation to the final conformation obtained after the simulation. The RMSD plot for the Aβ (1IYT) peptide in the simulated complex depicted in (**Figure 4.18B**) in blue colour was seen to be in the range of 0.25-1.25 nm which seems to be stabilized at 125 ns at 1.25 nm showing that it reached convergence, but is at higher RMSD value as expected, given that the Aβ (1IYT) is a small peptide of 42 amino acid residues. Likewise, The RMSD plot for the compound BD23 shown in (**Figure 4.18B**) in purple color seems to be in the range of 0.5-2 nm, as there are some fluctuations as the compound is constantly rearranging in the binding site with the Aβ in order to form a stable complex and reach its global energy minima. Root Mean Square Fluctuation (RMSF) is a commonly used analysis metric in MD simulations to analyze the flexibility and

stability of biomolecules.

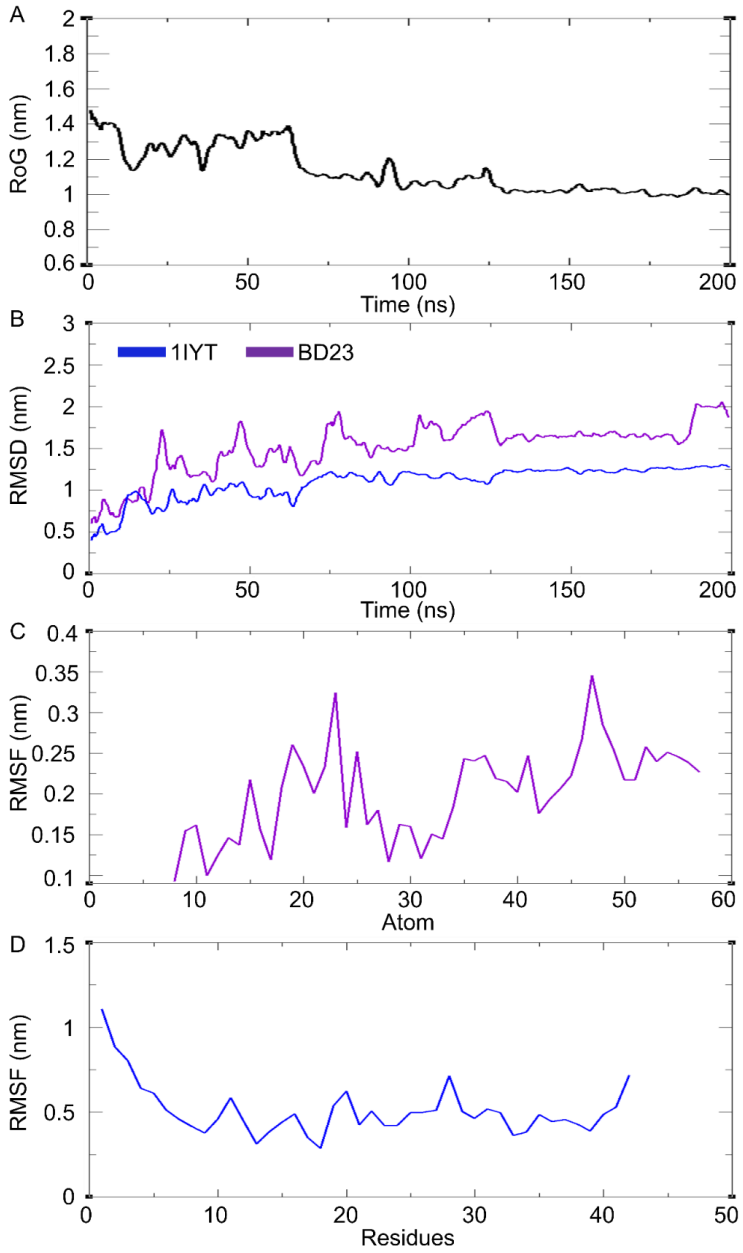

Figure 4.18. Molecular dynamics trajectory analysis of BD23-Aβ monomer complex. (A) Radiation of Gyration of the complex (B) RMSD (Root Mean Square Deviation protein), (C) RMSF (Root Mean Square Fluctuation) of ligand (D) RMSF of protein.

It provides information about the dynamic behavior of individual atoms or groups of atoms throughout the simulation. RMSF analysis provides insights into the crucial amino acid residues that are responsible for the dynamic behavior of biomolecules and can be used to study

conformational changes, protein-ligand interactions occurring during an MD simulation. The RMSF of the compound BD23 (**Figure 4.18C**) showed fluctuation in the range of 0.1 to 0.35 nm which explains the flexibility of the compound as a small molecule and the flexibility of the compound helps it to interact with the various amino acids of the Aβ monomer and thus form a stable complex. The RMSF of the Aβ (1IYT) protein (**Figure 4.18C**) have been found to fluctuate in between the range of 0. 25 to 1.2 nm that indicates the flexibility of the protein throughout the simulation period.

In order to better understand key interactions between the protein ligand interaction that might help in the stabilization of the formed complex, the number of hydrogen bonds formed during the MD simulation was analyzed. In general, the optimal distance for a hydrogen bond donor and acceptor is ≤3.5 Å (0.35 nm) with an angle of 180° ± 30°. Here we have investigated the average number of H-bond formation during the 200 ns simulation with the cut-off value set at 0.35 nm (**Figure 4.19A**). There seems to be several instances where there is no H-bond formation between BD23 and Aβ (1IYT) protein during the first 100 ns of the simulation followed by an average of 2 H-bond for the remaining time span of the 200 ns simulation. Hydrogen bond distance (HBD) shown in **(Figure 4.19B)** it can be noticed that the average H-bond distance was about 0.3 nm.

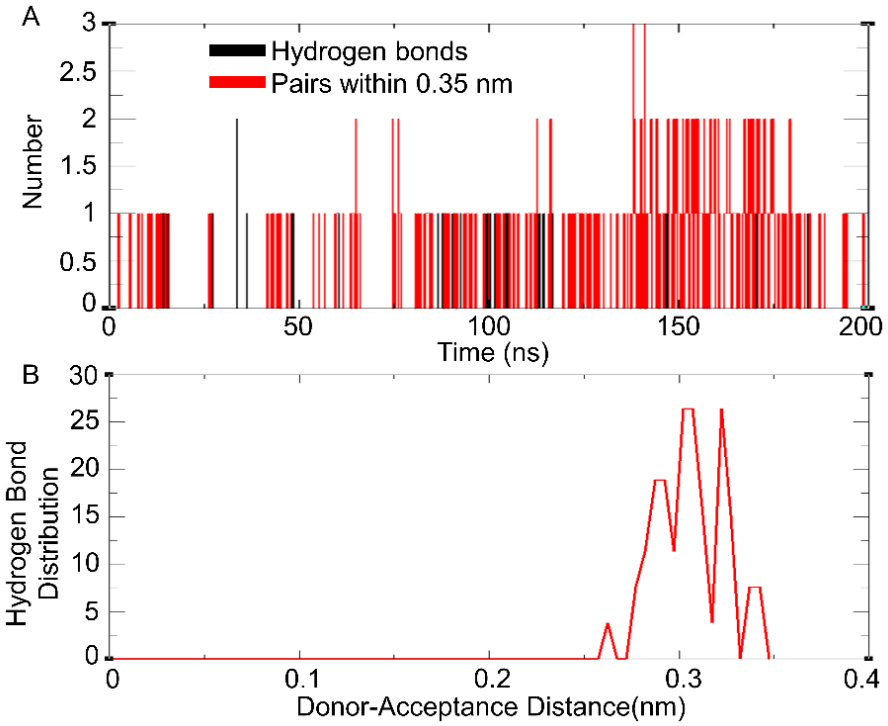

Figure 4.19. Hydrogen bond analysis of BD23-Aβ monomer complex MD trajectory. (A) Total number of H-bonds, and (B) Hydrogen bond distribution

4.3.10.2. Molecular dynamics of the BD23-Aβ pentamer (2BEG) complex

Further, to understand the interaction of BD23 with the Aβ pentamer, we have performed MD simulation for 200 ns of BD23-Aβ pentamer complex. The RoG value of the complex BD23 with pentamer of Aβ (PDB:2BEG) is depicted in (**Figure 4.20A**). A relatively high but stable RoG value within the range of 1.5-2 nm was observed as expected due to the small peptide nature of the protein having good flexibility and constantly evolving with respect to its three-dimensional structure during the complex formation and no abrupt motions observed during the 200 ns simulation. Furthermore, the RMSD of the simulated system was evaluated (**Figure 4.20B**), where the RMSD for the Aβ pentamer (2BEG) protein shown in blue colour seems to be in the range of 0.25-1.75 nm which seems to be increasing after the 75 ns of the simulation. Likewise, The RMSD plot for the compound BD23 shown in **(Figure 4.20B)** purple color was in the range of 0.5-2.25 nm, which seems to fluctuate after 125 ns. The RMSF plot for

compound BD23 shown in (**Figure 4.20C**) have been found to be in between 0.1-0.35 nm that indicates the flexibility of the ligand throughout the simulation period that helps it to rearrange in order to make a complex with the Aβ pentamer in order to form a stable complex and reach energy minima.

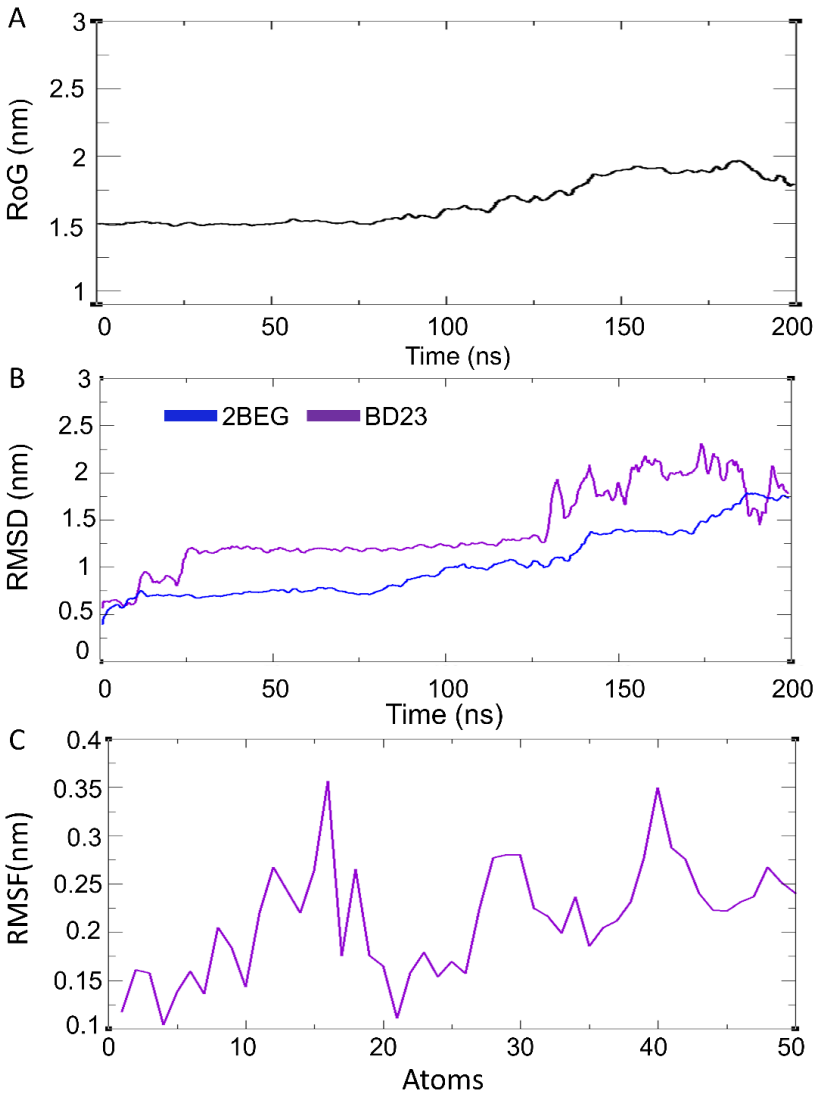

Figure 4.20. Molecular dynamics trajectory analysis of BD23-Aβ pentamer complex. (A) RoG (B)RMSD. (C) RMSF of ligand.

Also the average number of H-bond formation during the 200 ns simulation with the cut-off value set at 0.35 nm was evaluated for the BD23 with the pentamer of Aβ (PDB:2BEG) (**Figure 4.21A**). There seems to be several instances where there is no H-bond formation between BD23

and pentamer of Aβ (PDB:2BEG) during the 100-200 ns time interval of the simulation as well as there were no H-bond formation at the first 25 ns of the simulation, followed by an average of 1 H-bond for the remaining time span in between. Hydrogen bond distance (HBD) shown in (**Figure 4.21B**) it can be noticed that the average H-bond distance was about 0.3 nm.

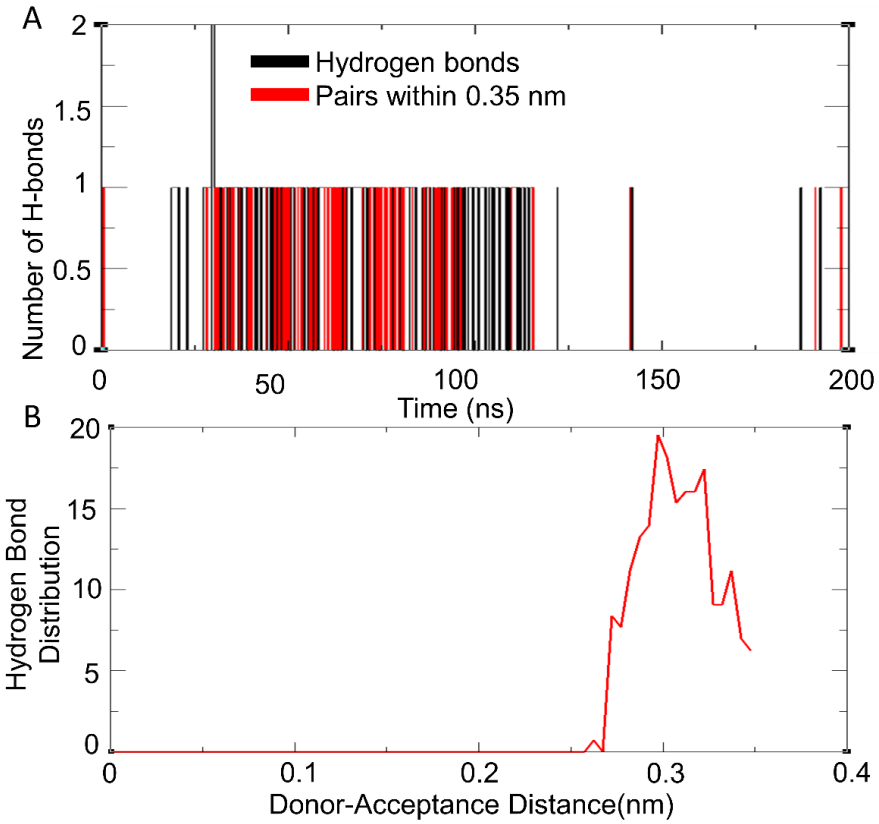

Figure 4.21. Hydrogen bond analysis of BD23-Aβ pentamer complex MD trajectory. (A) Total number of H-bonds, and (B) Hydrogen bond distribution**.**

4.3.10.3. Molecular Dynamics of BD23-tau monomer cluster 6 (C06) complex

We have also performed the simulation of the compound BD23 with the top scoring cluster C6 of tau protein. The evaluated parameters are shown in (**Figure 4.22**). The RoG value of the complex BD23 with C06 is shown in **(Figure 4.22A**) A relatively high RoG value in the range of 1.5-3 nm was observed as expected due to the small size of the tau protein and having good flexibility and was constantly evolving during the complex formation as it belongs to the intrinsically disordered proteins. There was no uncertainty observed during simulation time

frame. Furthermore, the RMSD of the simulated system was evaluated (**Figure 4.22B**), where the RMSD of cluster C06 shown in blue colour seems to be in the range of 0.25-1.75 nm which seems to be stable and denotes that the complex formation was taking place.

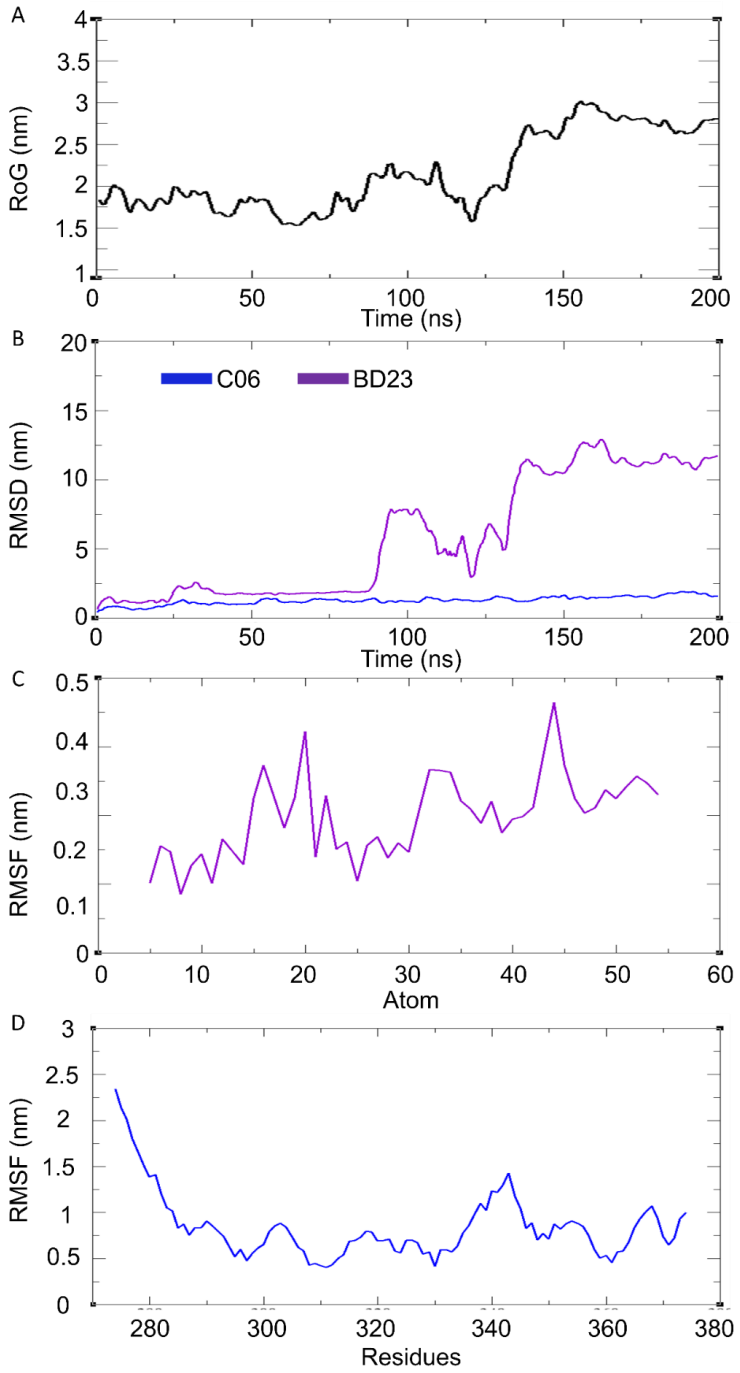

Figure 4.22. Molecular dynamics trajectory analysis of BD23-tau monomer cluster 6 complex. (A) RoG (B) RMSD (C) RMSF (D) RMSF of protein.

Likewise, The RMSD plot for the compound BD23 shown in (**Figure 4.22B**) purple colour was in the range of 1-12.5 nm, which seems to fluctuating greatly after the 80 ns of the simulation due to the flexible nature of the compound which results in constant adjustment in the binding process with the C06 tau protein in order to reach energy minima. The RMSF plot for compound BD23 shown in (**Figure 4.22C**) have been found to be in between 0.1-0.45 nm that indicates the flexibility of the ligand throughout the simulation period which helps it to rearrange in order to make a complex with the tau protein in order to form a stable complex and reach energy minima. Furthermore, the tau protein RMSF depicted in (**Figure 4.22D**) was observed in the range of 0.5-2.5 nm which is due to the nature of the tau protein as it belongs to the intrinsically disordered proteins and is a small protein system.

The average number of H-bond formation during the 200 ns simulation with the cut-off value set at 0.35 nm was calculated for the complex BD23-C06 tau complex **(Figure 4.23A).** There seems to be no H-bond formation between BD23 and C6 in between the 80-130 ns time interval of the simulation, followed by an average of 1-2 H-bond formation during the 200ns simulation. Hydrogen bond distance (HBD) shown in **(Figure 4.23B**) it can be seen that the average H-bond distance was maintained about 0.3 nm.

4.3.10.4. Molecular Dynamics of the BD23-tau monomer Cluster 8 (C08) complex

Likewise, the simulation for the compound BD23 with the tau monomer cluater 8 was also carried out and evaluated (**Figure 4.24**). The RoG value of the complex BD23 with C08 is depicted in (**Figure 4.24A**) and was observed in the range of 1.5-4 nm, where it can be seen from the graph that There is a sudden rise in RoG value but then was stable at 4 nm. There was no uncertainty observed during simulation time frame. Furthermore, the RMSD of the simulated system is shown in (**Figure 4.24B**), where the RMSD C08 protein represented in blue colour on the graph seems to be in the range of 0.25-1.75 nm which seems to be stable and denotes that the complex formation was taking place.

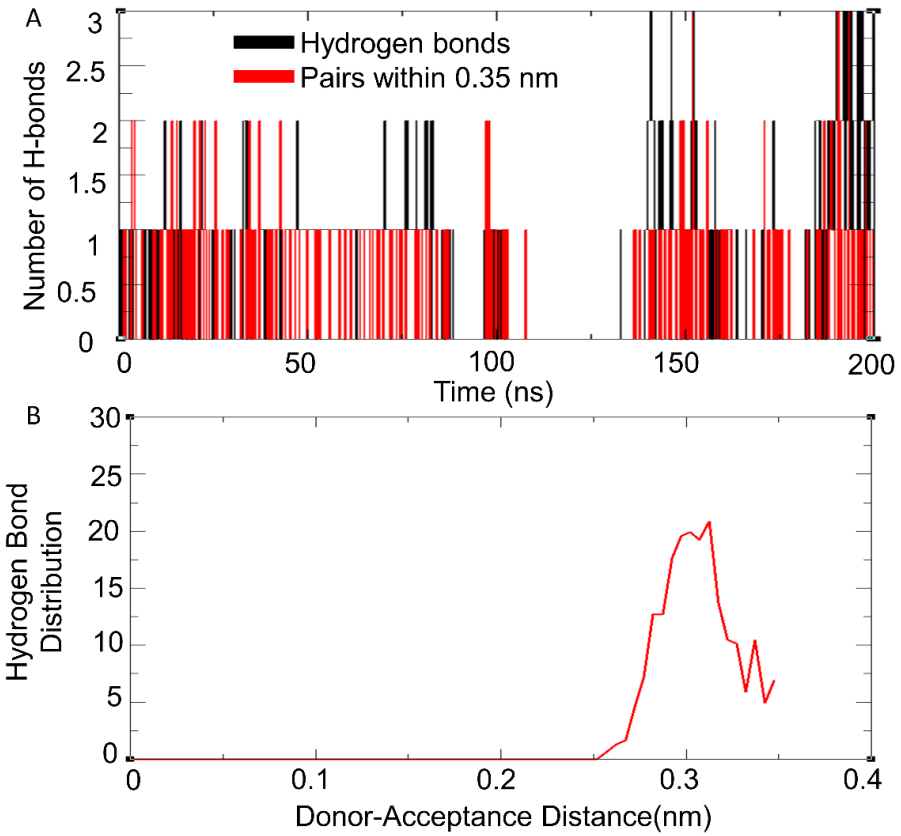

Figure 4.23. Hydrogen bond analysis of the BD23-tau monomer Cluster 6 complex. (A) Total number of H-bonds, and (B) Hydrogen bond distribution.

Likewise, The RMSD plot for the compound BD23 shown in (**Figure 4.24B**) purple colour was in the range of 1-20 nm, which seems to fluctuate greatly after the 80 ns of the simulation due to the flexible nature of the compound which results in a constant adjustment in the binding process with the C8 tau protein in order to reach energy minima. The RMSF plot for compound BD23 shown in (**Figure 4.24C**) was observed in the range of 0.1-0.35 nm indicating the flexibility of the ligand throughout the simulation period which helps it to rearrange in order to make a complex with the tau protein in order to form a stable complex and reach energy minima. Furthermore, tau monomer cluster 8 RMSF depicted in (**Figure 4.24D**) was observed in the range of 0.25-1.5 nm which is a bit high due to the flexibility of the protein.

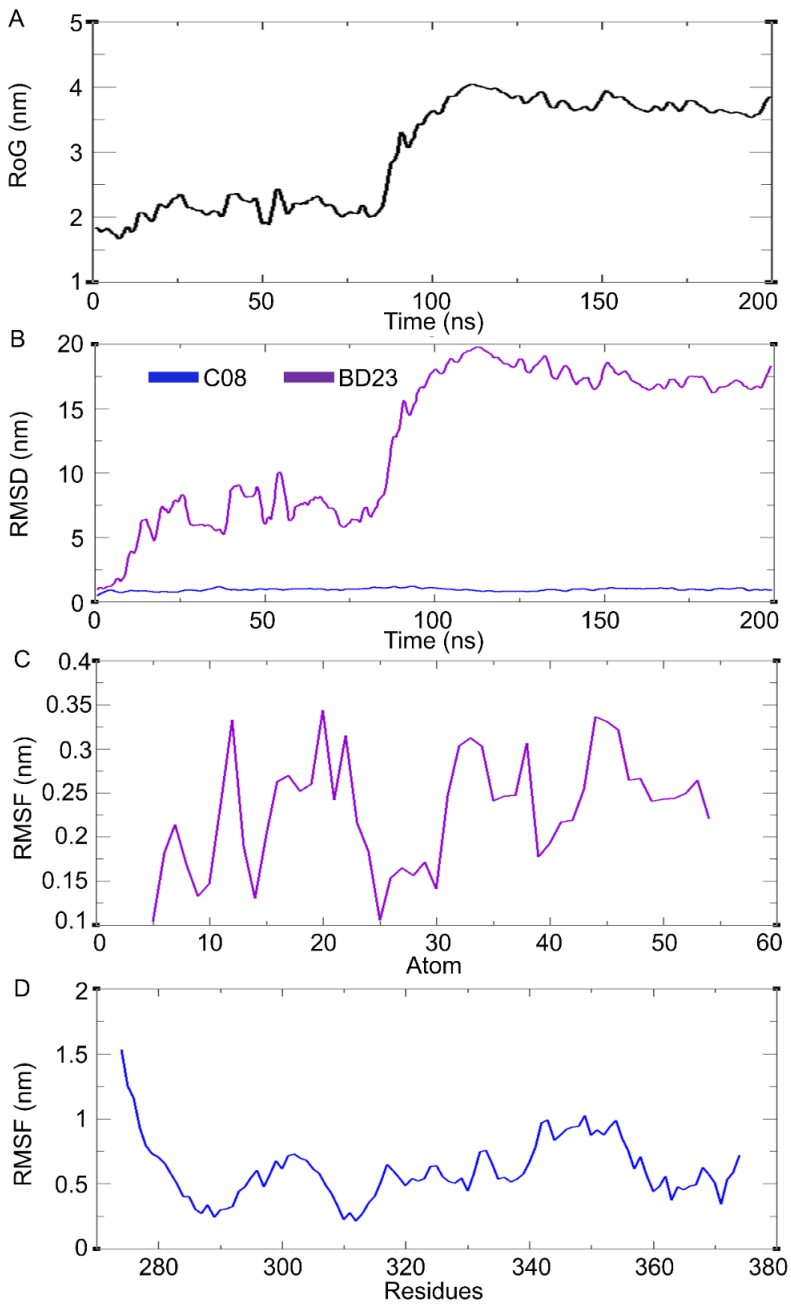

Figure 4.24. Molecular dynamics trajectory analysis of BD23-tau monomer cluster 8 complex. (A) RoG (B)RMSD, (C) RMSF of ligand, (D) RMSF of protein.

The average number of H-bond formation during the 200 ns simulation with the cut-off value set at 0.35 nm was estimated for BD23-tau monomer cluster 8 complex system (**Figure 4.25A**). There seems to be missing instances of H-bond formation between BD23 and C08 in between the first 100 ns time interval of the simulation, followed by an average of 1-2 H- bond formation

during the 200 ns simulation. Hydrogen bond distribution (HBD) shown in (**Figure 4.25B**) it can be seen that the average H-bond distance was maintained about 0.3 nm.

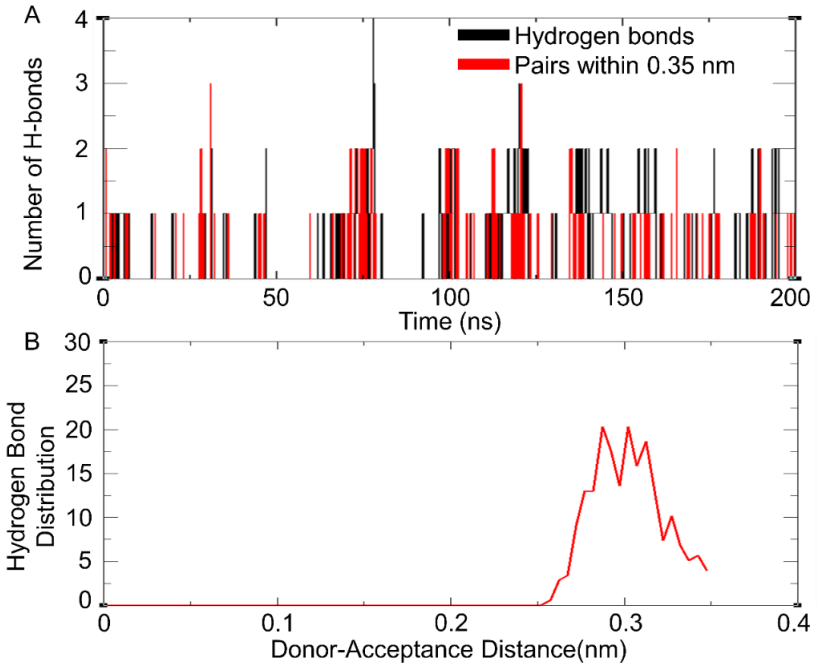

Figure 4.25. Hydrogen bond analysis of the compound BD23-tau monomer cluster 8 complex. (A) Total number of H-bonds, and (B) Hydrogen bond distribution.

Principal component analysis (PCA) is also known as "essential dynamics" and can identify the most crucial conformational degrees of freedom of the simulated system based on the principles of covariance matrix. It allows us to identify the major components of the system that together explains the overall motions of the protein. Thereby, allowing data reduction by the linear transformation of the original variables to a set of new concerted variables, which allows one to interpret the features of the data set from only few "principal components". We have performed the principal component analysis (PCA) for all the simulated system complexes. The eigenvalues of the first 10 principal components (eigenvectors) for BD23 with various Aβ and tau complexes are shown in (**Figure 4.26**).

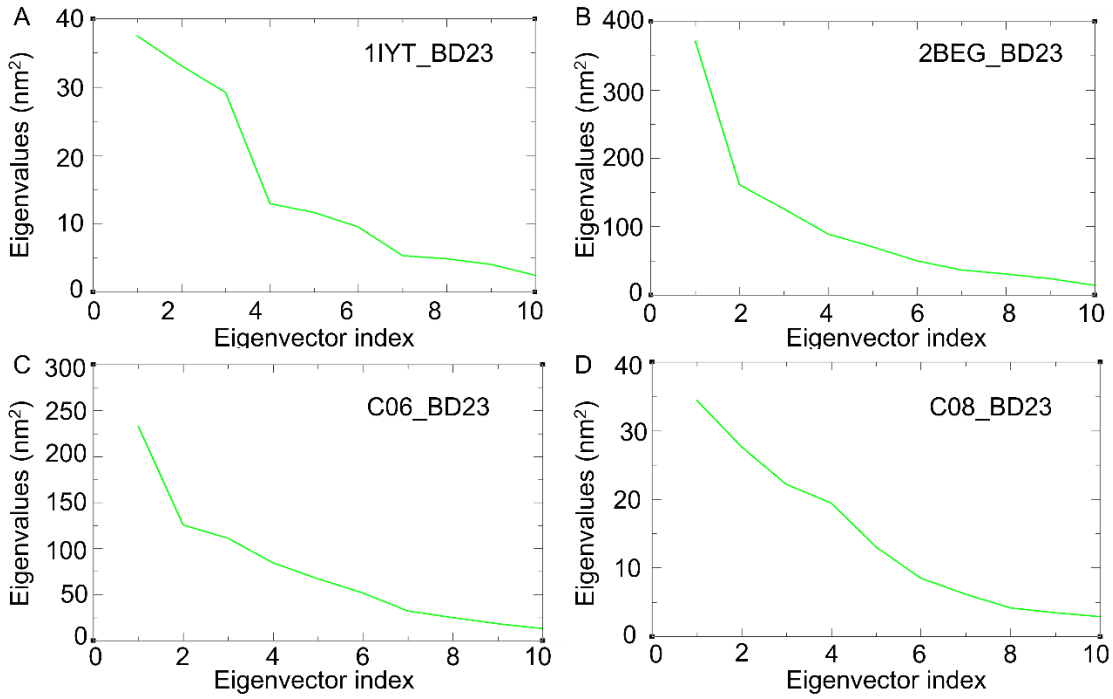

Figure 4.26. Eigenvalues of the first 10 principal components of the simulated system for the Aβ and tau clusters with the compound BD23. (A) Eigenvalues of the first principal components of the simulated system for the BD23-Aβ monomer complex (B) Eigenvalues of the first principal components of the simulated system for the BD23-Aβ pentamer complex (C) Eigenvalues of the first principal components of the simulated system for the BD23-C06 tau complex (D) Eigenvalues of the first principal components of the simulated system BD23-C08 tau. Here, the principal component analysis identifies the most contributing parameters that explain the structural stability of Aβ and tau complex during its interaction with the BD23.

These analyses showed that the first two components explained most of the variations in the data and then the graph slowly declines and becomes horizontal having the least explain ability. Finally, we used the first two principal components to plot the 2D PCA plot (**Figure 4.27**). The PCA graph denotes the various conformational changes that occurred during the complex formation. The 2D plot shows widespread distribution in the conformational space with stable clusters, most likely due to various conformational changes in the protein structure upon molecular interaction with the compound BD23, resulting in various stable conformational

states.

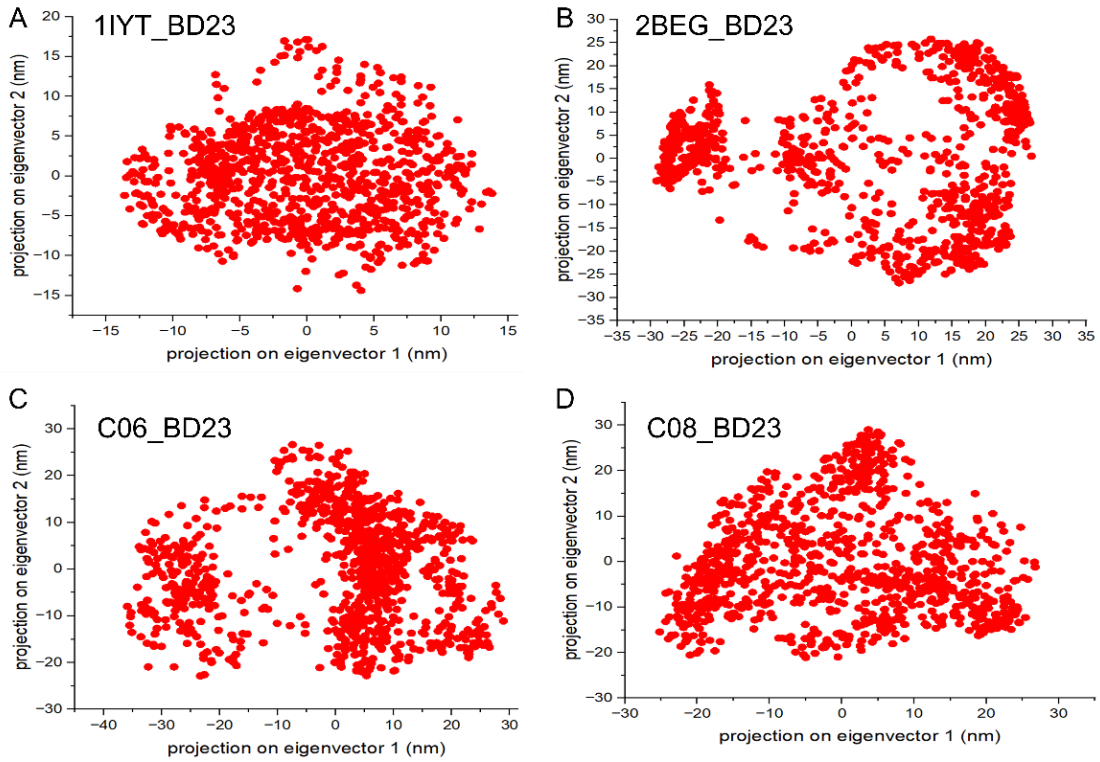

Figure 4.27. The 2D projection of the first two principal components for the BD23-Aβ monomer complex (A), BD23-Aβ pentamer complex (B), BD23-C06 tau complex (C), and BD23-C08 tau complex. Each dot on the plot is representation of a specific conformational state in the different amyloid beta and tau proteins with the ligand BD23 throughout the simulation. The spread represents the primary conformational changes in the Aβ and tau protein during the interaction of BD23 during the simulation. Overall, the graph represents a uniform widespread distribution of the conformational sampling for all the complexes.

4.3.11. Free Energy Landscape (FEL) Analysis

The free-energy landscape (FEL) analysis uses two variables that can directly reflect the specific properties of the system, namely here we have utilized the changes in the RMSD of the system versus RoG of the system. The FEL analysis therefore measures the stability of the conformational changes in relation to changes in the Gibbs free energy (ΔG) of the system.

FEL analysis thereby, plays a major role in understanding and unraveling the various biochemical processes. Here we have evaluated the energy minima landscape for the compound BD23 with various Aβ and tau complexes (**Figure 4.28**), based on the shape and size of the 2D and 3D projection on the graph. The color code bars in the figures refer to the various energy levels of the complexes during the simulation process. Like, in the 2D energy landscape, the centralized blue areas show the complex within the cluster with the least energy and hence the most conformation attained by the complex during the simulation. In the 3D projections, the narrow-shaped funnel illustrates the dynamic changes in conformations with respect to time for the system to reach a stable structure having the lowest energy.

The FEL analysis revealed that the ΔG values of the compound BD23-Aβ monomer complex (**Figure 4.28A**), converged to an energy minimum state which is illustrated in the overall 3D plots as a single funnel formation. This along with the 2D contour plot clearly illustrates that in the simulated system BD23 complexed with Aβ monomer (1IYT) protein reached a single distinct local energy minima and hence a stable folding state. However, an exception was observed for the BD23-Aβ pentamer complex system, BD23-C06 tau complex and BD23-C08 tau complex (**Figure 4.28B**, **4.28C** & **4.28D**) respectively where the 3D plot shows multiple distinct funnel formation, indicating that folding process is not too gradual in reaching the global energy minima.

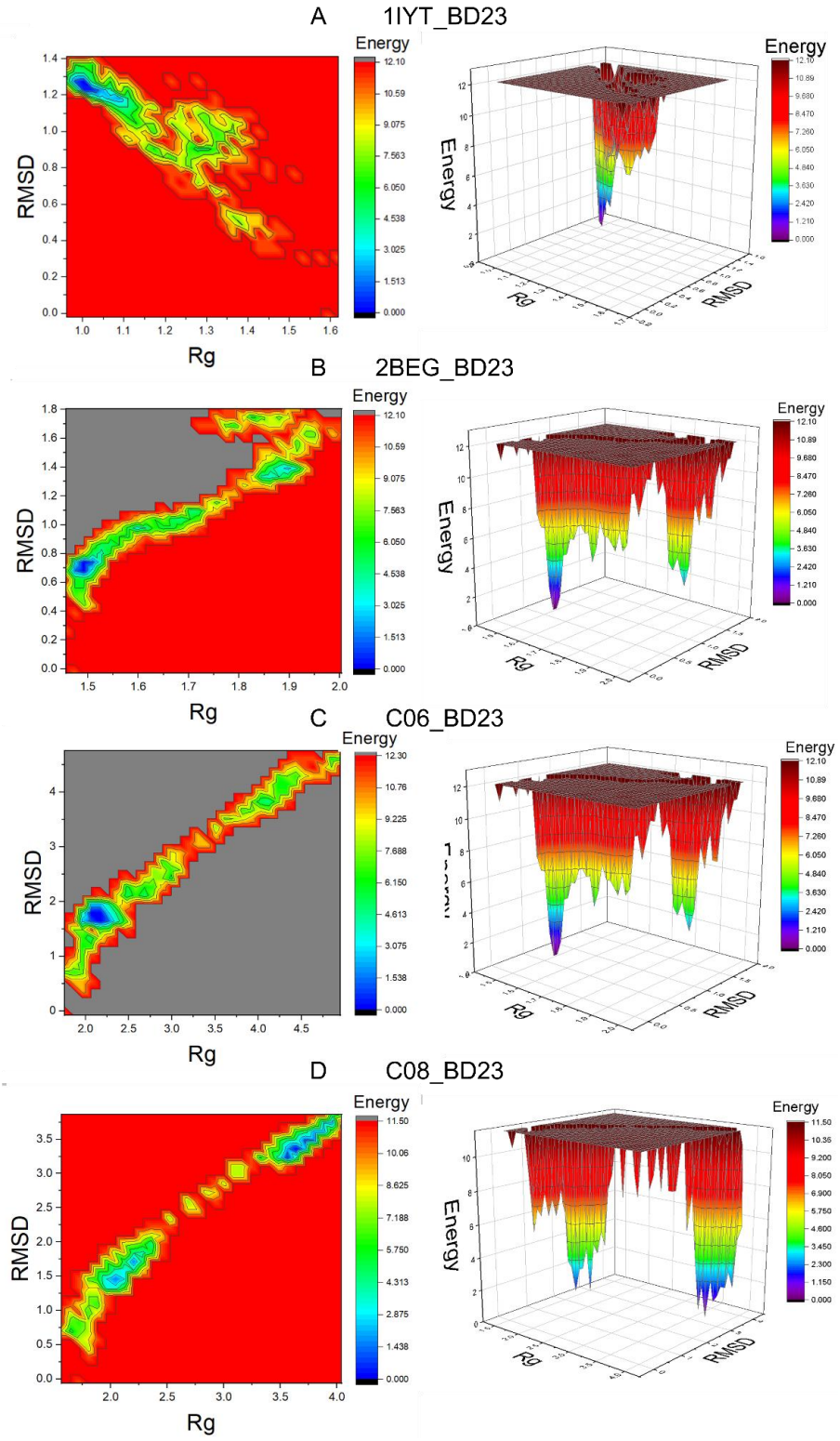

Figure 4.28. The 2D and 3D free energy landscape diagram as a function of RMSD and RoG as the two coordinates of the Aβ and tau complex with BD23. The free energy is displayed in terms of kj/mol where the purple colour indicates the least energy and red the highest energy. The folding funnel formed by the complex BD23 with Aβ monomer, pentamer,

cluster 06 of tau, and cluster 08 of tau shows stable folding. The complex BD23 showed less number of funnel in monomer than pentamer of Aβ and tau suggesting stability of the complex.

4.3.12. In Silico ADME

In drug development, ADME properties (Absorption, Distribution, Metabolism, and Excretion) are pivotal for determining the efficacy and safety profiles of potential drug candidates. Recently, in silico tools, such as the Swiss ADME webserver http://www.swissadme.ch/ have emerged as invaluable assets for predicting these properties. By employing these computational methods, researchers can significantly reduce experimental costs and expedite the drug discovery timeline. An examination of the pharmacokinetic properties, as delineated in **Table 4.6**, reveals intriguing patterns. The molecular weight of the compounds under investigation spans a range from 299.75 to 538.23 g/mol. These compounds also exhibit an average number of rotatable bonds, a factor often associated with molecular flexibility. Notably, the majority of these compounds adhere to Lipinski's Rule of Five, a guideline that predicts the "drug-likeness" of molecules based on certain physicochemical properties. However, exceptions were observed in the cases of compounds BD14, BD21, BD17, BD18, and BD19, which possess molecular weights exceeding the recommended threshold. From a structural perspective, all compounds demonstrated fewer than 10 hydrogen bond acceptors, in alignment with Lipinski's guidelines. Moreover, hydrogen bond donors were observed to be fewer than 5 across the board. An additional promising feature is the absence of Pan-Assay Interference Compounds (PAINS); all evaluated compounds yielded a zero value in this metric. Consistent with the Rule of Five, the Log P value for each compound remained below 5. Another critical observation pertains to the BBB permeability exhibited by all compounds. This feature, combined with favorable topological polar surface area (TPSA) readings and a bioavailability score of 0.55, suggests a promising pharmacokinetic profile for these molecules.

Table 4.6. ADME properties of the synthesized compounds calculated using Swiss ADME webserver.

Compounds	MW	Rotatable bonds	H-bond acceptor	H-bond donors	MR	TPSA	MLOGP	Bioavailability	PAINS alerts	BBB Permeability
BD01	317.74	6	3	1	83.61	46.17	3.34	0.55	0	Yes
BD02	299.75	6	2	1	83.65	46.17	2.96	0.55	0	Yes
BD03	247.68	5	2	1	66.94	46.17	2.13	0.55	0	Yes
BD04	329.78	7	3	1	90.14	55.4	2.61	0.55	0	Yes
BD05	371.02	5	2	1	77.33	46.17	2.9	0.55	0	Yes
BD06	281.23	6	5	1	66.93	46.17	2.51	0.55	0	Yes
BD07	351.29	7	6	1	83.6	46.17	3.69	0.55	0	Yes
BD08	333.3	7	5	1	83.64	46.17	3.31	0.55	0	Yes
BD09	414.88	7	5	0	117.33	59.08	2.21	0.55	0	Yes
BD10	356.85	6	2	0	107.02	40.62	2.74	0.55	0	Yes
BD11	482.95	8	5	0	135.67	40.62	4.44	0.55	0	Yes
BD12	357.83	6	3	0	104.81	53.51	2.1	0.55	0	Yes
BD13	446.97	8	3	0	135.76	40.62	3.71	0.55	0	Yes
BD14	538.23	7	5	0	127.72	59.08	2.9	0.55	0	Yes
BD15	480.19	6	2	0	117.41	40.62	3.45	0.55	0	Yes
BD16	481.18	6	3	0	115.2	53.51	2.81	0.55	0	Yes
BD17	508.25	6	2	0	127.34	40.62	3.86	0.55	0	Yes
BD18	606.3	8	5	0	146.06	40.62	5.09	0.17	0	Yes
BD19	505.2	6	3	0	122.12	64.41	2.75	0.55	0	Yes
BD20	448.43	8	8	0	117.32	59.08	2.52	0.55	0	Yes
BD21	516.5	9	8	0	135.66	40.62	4.73	0.17	0	No
BD22	390.4	7	5	0	107.01	40.62	3.07	0.55	0	Yes
BD23	415.41	7	6	0	111.73	64.41	2.38	0.55	0	Yes
BD24	418.45	7	5	0	116.94	40.62	3.49	0.55	0	Yes
BD25	391.39	7	6	0	104.81	53.51	2.43	0.55	0	Yes
BD26	480.52	9	6	0	135.75	40.62	4	0.55	0	Yes
BD27	369.88	7	2	0	109.26	37.38	3.76	0.55	0	Yes
BD28	493.23	7	2	0	119.65	37.38	4.45	0.55	0	Yes

MW: molecular weight; MR: molecular refractivity; TPSA: topological polar surface area; ILOGP, XLOGP3, WLOGP, and MLOGP are the predictive models of Swiss ADME and their values indicate lipophilicity of molecules.

4.4. Materials and Methods

4.4.1. Chemistry

All the reagents and chemicals used for the synthesis and characterization of compounds were purchased from Sigma-Aldrich, Alfa-Aesar, and SRL (Sisco Research Laboratories Pvt. ltd). The solvents were dried by standard solvent drying methods. The compounds were characterized by AVH D 500 AVANCE III HD 500 MHz OneBay NMR Spectrometer at IITBHU, and High-resolution mass spectra (HRMS) were obtained by electrospray (HRMS/ESI), recorded with Agilent1100 LC-Q-TOF and HRMS-6540-UHD machine at Department of Chemistry, Banaras Hindu University. All the structures were drawn by using ChemDraw Professional 16. For sample quantification, we used RP-HPLC Agilent 1260 infinity II. The NMR, HRMS spectra of all the compounds and HPLC calibration curve for quantification and percentage purity data of BD23 is given in **Annexure I (page no. 276-319).**

4.4.1.1. General procedure for the synthesis of γ-substituted β,γ-unsaturated α-keto thioesters (3a-c) and γ-Substituted β,γ-unsaturated α-hydroxy thioesters (4a-c).

Different α-keto thioesters are synthesized by reaction of different substituted benzaldehyde **1a-c** (1eq) with various Wittig salt (2 eq) in order to synthesize the benzylidene acetones **2a-c**. Further, the compounds **2a-c** reacted with DMSO and triphenylphosphine hydrobromide at 50 °C, when the reaction was completed; brine solution was added and the organic layer was separated. Then the reaction mixture was separated through column chromatography using 100-200 mesh size to obtain **3a-c**. γ-Substituted β,γ-unsaturated α-keto thioesters **3a-**c (0.05 g, 1 equiv) were dissolved in dry DCM (1.0 mL), and triethyl silane (Et_3SiH; 2.5 equiv) and $BF_3.OEt_2$ (1.0 equiv) was added successively to the reaction mixture and allowed to stir at room temperature for 15-40 min under an nitrogen atmosphere. After completion of the reaction (TLC), water was added, and the product was extracted with DCM. The combined organic layers were dried over anhydrous Na_2SO_4 and filtered, and the filtrate was concentrated under

reduced pressure to get a residue. The crude residue was purified over silica gel column chromatography [100−200 mesh; eluent: ethyl acetate/n-hexane] to obtain **4a-c**.

4.4.1.2. General procedure for the synthesis of β,γ-unsaturated α-ketoamides (BD01 to BD08)

γ-Substituted β, γ-unsaturated *α*-ketothioester*:* **3a-c** (0.05 g, 1.0 eq) was dissolved in dry toluene (1.0 mL), and the respective amine (3.0 eq) was added to the reaction mixture. The reaction mixture was allowed to stir at room temperature for 25- 30 min. After completion of the reaction, brine solution was added, and the product was extracted with DCM. The combined organic layers were dried over anhydrous Na_2SO_4 and filtered, and the filtrate was concentrated under reduced pressure to get a residue. The crude residue was purified over silica gel column chromatography [100−200], eluent: ethyl acetate/n-hexane] to obtain the pure product.

4.4.1.2.1. (*E*)-4-(4-chlorophenyl)-N-(4-fluorobenzyl)-2-oxobut-3-enamide (**BD01**)

Yellow solid, 55 % yield. **^{1}H NMR (500 MHz, $CDCl_3$): δ** 7.92 (d, *J* = 16.2 Hz, 1H), 7.78 (d, *J* = 16.0 Hz, 1H), 7.63 (d, *J* = 9.2 Hz, 2H), 7.49 (s, 1H), 7.43 (d, *J* = 8.5 Hz, 2H), 7.32 (d, *J* = 7.9 Hz, 2H), 7.10 – 7.03 (m, 2H), 4.53 (d, *J* = 6.3 Hz, 2H). **^{13}C NMR (126 MHz, $CDCl_3$)**: δ 185.12, 163.38, 161.05, 146.67, 137.64, 132.87, 132.82, 130.29, 129.69, 129.63, 129.43, 118.99, 115.83, 115.66, 42.86, 29.71. **HRMS (ESI)**: *m/z* calculated for $C_{17}H_{13}ClFNO_2$ $[M+H]^+$ = 318.0697; found : 318.0697

4.4.1.2.2. (*E*)-N-benzyl-4-(4-chlorophenyl)-2-oxobut-3-enamide (**BD02**)

Yellow solid, 55 % yield. **^{1}H NMR (500 MHz, $CDCl_3$): δ** 7.92 (d, *J* = 16.0 Hz, 1H), 7.79 (d, *J* = 16.2 Hz, 1H), 7.63 (d, *J* = 8.5 Hz, 2H), 7.49 (s, 1H), 7.42 (d, *J* = 8.5 Hz, 2H), 7.37 (d, *J* = 8.1 Hz, 2H), 7.34 (d, *J* = 7.5 Hz, 3H), 4.57 (d, *J* = 6.1 Hz, 2H). **^{13}C NMR (126 MHz, $CDCl_3$): δ** 185.21, 161.05, 146.53, 137.57, 137.04, 132.86, 130.29, 129.41, 128.87, 127.92, 127.89, 119.09, 43.59, 29.72, 22.71, 14.14. **HRMS (ESI): *m/z*** calculated for $C_{17}H_{14}ClNO_2$ $[M+H]^+$ =

300.0791, found : 300.0795

4.4.1.2.3. (*E*)-4-(4-chlorophenyl)-2-oxo-N-(prop-2-yn-1-yl)but-3-enamide (**BD03**)

Yellow solid, 52 % yield. **^{1}H NMR (500 MHz, $CDCl_3$): δ** 7.92 (d, *J* = 16.1 Hz, 1H), 7.73 (d, *J* = 16.2 Hz, 1H), 7.66 – 7.59 (m, 2H), 7.44 – 7.41 (m, 2H), 7.40 – 7.35 (m, 1H), 7.31 (s, 1H), 4.17 (dd, *J* = 5.6, 2.6 Hz, 2H). ^{13}C NMR (126 MHz, $CDCl_3$): δ 184.54, 160.77, 146.82, 137.68, 132.78, 130.31, 129.14, 118.85, 72.33, 29.23. **HRMS (ESI):** *m/z* calculated for $C_{13}H_{11}ClNO_2$ $[M+H]^+$ = 248.0478, found : 248.0487

4.4.1.2.4. (*E*)-4-(4-chlorophenyl)-N-(4-methoxybenzyl)-2-oxobut-3-enamide (**BD04**)

Yellow solid, 50 % yield. **^{1}H NMR (500 MHz, $CDCl_3$): δ** 7.88 (d, *J* = 16.2 Hz, 1H), 7.76 (d, *J* = 16.0 Hz, 1H), 7.61 (d, *J* = 9.2 Hz, 2H), 7.43 – 7.38 (m, 3H), 7.25 – 7.23 (m, 2H), 6.91 – 6.84 (m, 2H), 4.47 (d, *J* = 6.0 Hz, 2H), 3.80 (s, 3H). **^{13}C NMR (126 MHz, $CDCl_3$): δ** 185.28, 160.92, 159.31, 146.47, 137.55, 132.87, 130.28, 129.41, 129.36, 129.10, 119.08, 114.23, 55.34, 43.09, 31.95, 29.72, 29.68, 29.39, 22.72, 14.15, 1.04. **HRMS** (ESI): *m/z* calculated for $C_{18}H_{17}ClNO_3Na$ $[M+Na]^+$: 352.0716; found : 352.0715

4.4.1.2.5. (*E*)-4-(2,5-dibromophenyl)-2-oxo-N-(prop-2-yn-1-yl)but-3-enamide (**BD05**)

Yellow solid, 58 % yield. **^{1}H NMR (500 MHz, CDCl3): δ** 8.24 (d, J = 16.1 Hz, 1H), 7.92 (d, J = 2.3 Hz, 1H), 7.69 (d, J = 16.1 Hz, 1H), 7.52 (d, J = 8.5 Hz, 1H), 7.41 (dd, J = 9.6, 3.5 Hz, 1H), 7.36 (s, 1H), 4.19 (dd, J = 5.6, 2.6 Hz, 2H), 2.32 (s, 1H). **^{13}C NMR (126 MHz, $CDCl_3$): δ** 184.27 (s), 160.45 (s), 144.77 (s), 136.04 (s), 134.94 (d, *J* = 9.3 Hz), 134.26 (s), 131.84 (d, *J* = 19.3 Hz), 131.00 (s), 125.05 (s), 121.82 (d, *J* = 6.3 Hz), 72.42 (s), 43.53 (s), 42.50 (s), 29.27 (s), 14.36 (s). **HRMS (ESI)**: *m/z* calculated for $C_{13}H_9Br_2NO_2$ $[M+H]^+$ = 371.9058, found : 371.9054

4.4.1.2.6. (*E*)-4-(2,5-dibromophenyl)-N-(4-fluorobenzyl)-2-oxobut-3-enamide (**BD06**)

Yellow solid, 50 % yield. **^{1}H NMR (500 MHz, $CDCl_3$): δ** 8.23 (d, *J* = 16.1 Hz, 2H), 7.94 (s, 2H), 7.74 (d, *J* = 16.1 Hz, 2H), 7.52 (d, *J* = 8.5 Hz, 2H), 7.31 (dd, *J* = 9.2, 2.7 Hz, 5H), 7.06 (t, *J* = 7.6 Hz, 6H), 4.54 (d, *J* = 6.2 Hz, 4H). **^{13}C NMR (126 MHz, $CDCl_3$): δ** 136.10, 134.93, 133.40, 132.83, 129.59, 125.08, 124.91, 121.82, 115.92, 29.50. **HRMS (ESI)**: *m/z* calculated for $C_{17}H_{12}Br_2FNO_2$ $[M+H]^+$ = 441.9277, found : 441.9294

4.4.1.2.7. (*E*)-N-(4-fluorobenzyl)-2-oxo-4-(4-(trifluoromethyl)phenyl)but-3-enamide (**BD07**)

Yellow solid, 52 % yield. **^{1}H NMR (500 MHz, $CDCl_3$): δ** 7.97 (d, *J* = 16.2 Hz, 1H), 7.87 (d, *J* = 16.3 Hz, 1H), 7.80 (d, *J* = 8.0 Hz, 2H), 7.71 (d, *J* = 8.1 Hz, 2H), 7.48 (s, 1H), 7.35 – 7.29 (m, 2H), 7.11 – 7.04 (m, 2H), 4.54 (d, *J* = 6.2 Hz, 2H). **^{13}C NMR (126 MHz, $CDCl_3$): δ** 185.15, 160.82, 145.99, 137.58, 129.72, 129.65, 129.19, 126.05, 126.02, 120.79, 115.87, 115.69, 42.90, 31.95, 29.72, 29.38, 27.11, 22.71, 14.14. **HRMS (ESI)**: *m/z* calculated for $C_{18}H_{14}F_4NO_2$ $[M+H]^+$ = 352.0961, found : 352.0963

4.4.1.2.8. (*E*)-N-benzyl-2-oxo-4-(4-(trifluoromethyl)phenyl)but-3-enamide (**BD08**)

Yellow solid, 52 % yield . **^{1}H NMR (500 MHz, $CDCl_3$): δ** 7.94 (d, *J* = 16.3 Hz, 1H), 7.85 (d, *J* = 16.2 Hz, 1H), 7.77 (d, *J* = 8.4 Hz, 2H), 7.68 (d, *J* = 8.5 Hz, 2H), 7.46 (s, 1H), 7.39 – 7.28 (m, 5H), 4.55 (d, *J* = 6.1 Hz, 2H). **^{13}C NMR (126 MHz, $CDCl_3$): δ** 185.24, 160.82, 145.87, 136.94, 129.18, 128.90, 128.68, 128.56, 128.16, 127.95, 127.72, 127.60, 126.04, 126.00, 120.89, 43.63, 31.94, 29.72, 29.68, 29.38, 22.71, 14.14, 1.04. **HRMS (ESI): *m/z*** calculated for $C_{18}H_{14}F_3NO_2$ $[M+H]^+$ = 334.1055, found : 334.1058

4.4.1.3. General procedure for the synthesis of β,γ-saturated α-ketoamides (BD09 to BD28)

β,γ-Unsaturated *α*-hydroxy thioesters*:* **4a-c** (0.05 g, 1.0 equiv) was dissolved in dry toluene (1.0 mL), and respective (3.0 equiv) was added to the reaction mixture. The reaction mixture was allowed to stir at room temperature for 20- 30 min. After completion of the reaction, water was added, and the product was extracted with DCM. The combined organic layers were dried

over anhydrous Na_2SO_4 and filtered, and the filtrate was concentrated under reduced pressure to get a residue. The crude residue was purified over silica gel column chromatography [100−200], eluent: ethyl acetate/n-hexane] to obtain the pure product.

4.4.1.3.1. 1-(4-(benzo[d][1,3]dioxol-5-ylmethyl)piperazin-1-yl)-4-(4-chlorophenyl)butane-1,2-dione (**BD09**)

Light yellow gummy, 87 % yield**.** **^{1}H NMR (500 MHz, $CDCl_3$): δ** 7.29 – 7.23 (m, 2H), 7.18 – 7.12 (m, 2H), 6.84 (d, *J* = 1.6 Hz, 1H), 6.79 – 6.70 (m, 2H), 5.96 (s, 2H), 3.62 (dd, *J* = 6.4, 4.0 Hz, 2H), 3.43 (s, 2H), 3.30 (dd, *J* = 5.9, 4.2 Hz, 2H), 3.11 (t, *J* = 7.3 Hz, 2H), 2.96 (t, *J* = 7.3 Hz, 2H), 2.45 (t, *J* = 5.1 Hz, 2H), 2.34 (t, *J* = 5.1 Hz, 2H). **^{13}C NMR (126 MHz, $CDCl_3$): δ** 199.91, 164.94, 147.78, 146.88, 138.62, 132.13, 131.11, 129.77, 128.67, 122.29, 109.37, 107.97, 101.00, 62.46, 52.82, 52.17, 45.53, 41.58, 41.17, 28.25. **HRMS (ESI):** *m/z* calculated for $C_{22}H_{23}ClN_2O_4$ $[M+H]^+$ = 415.14; found : 415.1376

4.4.1.3.2. 4-(4-chlorophenyl)-1-(4-phenylpiperazin-1-yl) butane-1,2-dione (**BD10**)

White solid, 90 % yield. **^{1}H NMR (500 MHz, $CDCl_3$): δ** 7.34 – 7.29 (m, 3H), 7.28 (d, *J* = 2.0 Hz, 1H), 7.20 – 7.16 (m, 2H), 6.98 – 6.91 (m, 3H), 3.81 – 3.76 (m, 2H), 3.52 – 3.47 (m, 2H), 3.24 – 3.20 (m, 2H), 3.17 (t, *J* = 7.3 Hz, 2H), 3.10 (dd, *J* = 6.2, 4.1 Hz, 2H), 3.00 (t, *J* = 7.3 Hz, 2H). **^{13}C NMR (126 MHz, $CDCl_3$): δ** 199.75, 164.83, 150.72, 138.59, 132.20, 129.79, 129.33, 128.71, 120.95, 116.93, 49.87, 49.46, 45.48, 41.64, 41.19, 28.30. **HRMS (ESI):** *m/z* calculated for $C_{20}H_{21}ClN_2O_2$ $[M+H]^+$ = 357.1370; found : 357.1327

4.4.1.3.3. 1-(4-(bis(4-fluorophenyl)methyl)piperazin-1-yl)-4-(4-chlorophenyl)butane-1,2-dione (**BD11**)

Pale yellow solid, 88 % yield .**^{1}H NMR (500 MHz, $CDCl_3$): δ** 7.37 – 7.31 (m, 4H), 7.27 – 7.23 (m, 2H), 7.17 – 7.12 (m, 2H), 7.04 – 6.98 (m, 4H), 4.25 (s, 1H), 3.65 – 3.60 (m, 2H), 3.35 – 3.29 (m, 2H), 3.10 (t, *J* = 7.5 Hz, 2H), 2.95 (t, *J* = 7.3 Hz, 2H), 2.40 (t, *J* = 5.1 Hz, 2H), 2.27

(t, *J* = 5.0 Hz, 2H). **^{13}C NMR (126 MHz, $CDCl_3$): δ** 199.80, 164.80, 162.97, 161.01, 138.59, 137.33, 137.31, 132.14, 129.73, 129.24, 129.17, 128.67, 115.75, 115.58, 74.17, 51.78, 51.14, 45.66, 41.71, 41.10, 31.94, 29.71, 29.37, 28.29, 14.13. **HRMS (ESI):** m/z calculated for $C_{27}H_{26}ClF_2N_2O_2$ [M+H]+ = 483.1651; found : 483.1635

4.4.1.3.4. 4-(4-chlorophenyl)-1-(4-(pyridin-2-yl)piperazin-1-yl)butane-1,2-dione (**BD12**)

Light yellow gummy, 83 % yield. **^{1}H NMR (500 MHz, $CDCl_3$): δ** 8.22 (ddd, *J* = 4.9, 2.0, 0.9 Hz, 1H), 7.54 (ddd, *J* = 8.9, 7.2, 2.0 Hz, 1H), 7.29 (d, *J* = 2.1 Hz, 1H), 7.27 (s, 1H), 7.22 – 7.15 (m, 2H), 6.71 (ddd, *J* = 7.2, 4.9, 0.9 Hz, 1H), 6.66 (dt, *J* = 8.5, 1.1 Hz, 1H), 3.78 – 3.72 (m, 2H), 3.64 – 3.59 (m, 2H), 3.53 (dd, *J* = 6.6, 3.0 Hz, 2H), 3.50 – 3.44 (m, 2H), 3.17 (t, *J* = 7.4 Hz, 2H), 2.99 (t, *J* = 7.3 Hz, 2H). **^{13}C NMR (126 MHz, $CDCl_3$): δ** 199.67, 164.95, 158.84, 148.07, 138.58, 137.78, 132.21, 129.76, 128.70, 114.24, 107.32, 45.52, 45.23, 44.97, 41.43, 41.18, 31.94, 29.71, 29.67, 29.37, 28.29, 22.70, 14.13. **HRMS (ESI):** m/z calculated for $C_{19}H_{20}ClN_3O_2$ $[M+H]^+$ = 358.1322; found : 358.1308

4.4.1.3.5. 1-(4-benzhydrylpiperazin-1-yl)-4-(4-chlorophenyl)butane-1,2-dione (**BD13**)

White solid, 86% yield. **^{1}H NMR (500 MHz, $CDCl_3$): δ** 7.42 (d, *J* = 1.6 Hz, 2H), 7.40 (q, *J* = 1.7 Hz, 2H), 7.30 (dd, *J* = 8.4, 7.0 Hz, 4H), 7.28 – 7.20 (m, 3H), 7.18 – 7.12 (m, 2H), 4.26 (s, 1H), 3.70 – 3.58 (m, 2H), 3.39 – 3.30 (m, 2H), 3.09 (t, *J* = 7.5 Hz, 2H), 2.94 (t, *J* = 7.4 Hz, 2H), 2.43 (t, *J* = 5.2 Hz, 2H), 2.35 – 2.29 (m, 2H). **^{13}C NMR (126 MHz, $CDCl_3$): δ** 199.86, 164.88, 141.82, 138.60, 132.13, 129.92, 129.72, 128.68, 128.66, 128.60, 127.84, 127.29, 75.83, 51.92, 51.27, 45.75, 41.77, 41.15, 28.27. **HRMS (ESI)**: m/z calculated for $C_{27}H_{27}ClN_2O_2$ $[M+H]^+$ = 447.1839; found : 447.1825

4.4.1.3.6. 1-(4-(benzo[d][1,3]dioxol-5-ylmethyl)piperazin-1-yl)-4-(2,5 dibromophenyl)butane-1,2-dione (**BD14**)

White solid, 87 % yield. **^{1}H NMR (500 MHz, $CDCl_3$): δ** 7.43 – 7.37 (m, 2H), 7.22 (dd, *J* =

8.5, 2.4 Hz, 1H), 6.84 (d, *J* = 1.7 Hz, 1H), 6.80 – 6.71 (m, 2H), 5.96 (s, 2H), 3.69 – 3.61 (m, 2H), 3.44 (s, 2H), 3.44 – 3.38 (m, 2H), 3.17 – 3.10 (m, 2H), 3.05 (d, *J* = 13.9 Hz, 2H), 2.47 (t, *J* = 5.2 Hz, 2H), 2.42 (t, *J* = 5.1 Hz, 2H). **^{13}C NMR (126 MHz, $CDCl_3$): δ** 199.37, 164.79, 147.78, 146.87, 141.64, 134.27, 133.27, 131.20, 131.17, 122.97, 122.25, 121.36, 109.35, 107.97, 100.99, 62.46, 52.93, 52.19, 45.65, 41.66, 39.46, 31.93, 29.71, 29.37, 29.24, 22.71, 14.15. **HRMS (ESI):** m/z calculated for $C_{22}H_{22}Br_2N_2O_4$ $[M+H]^+$ = 539.004; found : 538.9961

4.4.1.3.7. 4-(2,5-dibromophenyl)-1-(4-phenylpiperazin-1-yl)butane-1,2-dione (**BD15**)

White solid, 90 % yield. **^{1}H NMR (500 MHz, $CDCl_3$): δ** 7.46 – 7.40 (m, 2H), 7.34 – 7.29 (m, 2H), 7.24 (dd, *J* = 8.5, 2.4 Hz, 1H), 6.99 – 6.93 (m, 3H), 3.81 (dd, *J* = 6.1, 4.3 Hz, 2H), 3.60 (t, *J* = 5.1 Hz, 2H), 3.24 (dd, *J* = 6.4, 3.9 Hz, 2H), 3.19 (q, *J* = 6.7, 4.9 Hz, 4H), 3.09 (t, *J* = 7.5 Hz, 2H). **^{13}C NMR (126 MHz, $CDCl_3$): δ** 199.22, 164.66, 150.74, 141.63, 134.32, 133.30, 131.24, 129.32, 122.99, 121.38, 120.94, 116.94, 49.99, 49.46, 45.59, 41.71, 39.48, 29.30. **HRMS (ESI):** *m/z* calculated for $C_{20}H_{21}Br_2N_2O_2$ $[M+H]^+$: 478.9970; found : 478.9962

4.4.1.3.8. 4-(2,5-dibromophenyl)-1-(4-(pyridin-2-yl)piperazin-1-yl)butane-1,2-dione (**BD16**)

White solid, 90 % yield. **^{1}H NMR (500 MHz, $CDCl_3$): δ** 8.20 (ddd, *J* = 4.9, 2.1, 0.9 Hz, 1H), 7.52 (ddd, *J* = 8.9, 7.2, 2.0 Hz, 1H), 7.43 – 7.38 (m, 2H), 7.21 (dd, *J* = 8.5, 2.4 Hz, 1H), 6.72 – 6.63 (m, 2H), 3.77 – 3.72 (m, 2H), 3.62 – 3.56 (m, 4H), 3.54 (td, *J* = 4.9, 2.4 Hz, 2H), 3.20 – 3.14 (m, 2H), 3.06 (t, *J* = 7.7 Hz, 2H). **^{13}C NMR (126 MHz, $CDCl_3$): δ** 199.17, 164.78, 158.84, 148.07, 141.61, 137.79, 134.31, 133.31, 131.24, 122.98, 121.38, 114.24, 107.32, 45.58, 45.33, 44.99, 41.49, 39.48, 31.94, 29.71, 29.67, 29.37, 29.29, 22.70, 14.13. **HRMS (ESI)**: m/z calculated for $C_{19}H_{19}Br_2N_3O_2$ $[M+H]^+$ = 481.9902; found : 481.9886

4.4.1.3.9. 4-(2,5-dibromophenyl)-1-(4-(2,5-dimethylphenyl)piperazin-1-yl)butane-1,2-dione (**BD17**)

White solid, 95 % yield. **^{1}H NMR (500 MHz, $CDCl_3$): δ** 7.46 – 7.38 (m, 2H), 7.22 (dd, *J* =

8.5, 2.4 Hz, 1H), 7.08 (d, *J* = 7.6 Hz, 1H), 6.84 (d, *J* = 9.6 Hz, 1H), 6.79 (s, 1H), 3.77 (s, 2H), 3.56 – 3.51 (m, 2H), 3.17 (t, *J* = 7.6 Hz, 2H), 3.07 (t, *J* = 7.7 Hz, 2H), 2.92 (t, *J* = 5.0 Hz, 2H), 2.87 (s, 2H), 2.30 (s, 3H), 2.26 (s, 3H). **^{13}C NMR (126 MHz, $CDCl_3$): δ** 199.41, 165.02, 150.41, 141.66, 136.38, 134.30, 133.32, 131.23, 131.04, 129.46, 124.68, 122.99, 121.39, 120.15, 52.08, 51.57, 46.29, 42.25, 39.54, 31.94, 29.71, 29.67, 29.38, 29.29, 22.71, 21.15, 17.35, 14.14. **HRMS (ESI):** m/z calculated for $C_{22}H_{24}Br_2N_2O_2$ $[M+H]^+$ = 509.0262; found : 509.0241

4.4.1.3.10. 1-(4-(bis(4-fluorophenyl) methyl) piperazin-1-yl)-4-(2,5-dibromophenyl)butane-1,2-dione (**BD18**)

Prepared according to the general procedure discussed above: Rf = 0.3; eluent, EtOAc/n-hexane (15%); light yellow liquid (0.043 g, 85%). **^{1}H NMR (500 MHz, $CDCl_3$): δ** 7.41 (d, *J* = 3.4 Hz, 1H), 7.38 (s, 1H), 7.38 – 7.33 (m, 4H), 7.21 (dd, *J* = 8.5, 2.4 Hz, 1H), 7.04 – 6.98 (m, 4H), 4.28 (s, 1H), 3.68 – 3.63 (m, 2H), 3.46 – 3.41 (m, 2H), 3.16 – 3.10 (m, 2H), 3.03 (t, *J* = 7.8 Hz, 2H), 2.43 (t, *J* = 5.2 Hz, 2H), 2.39 – 2.35 (m, 2H). **^{13}C NMR (126 MHz, $CDCl_3$): δ** 199.28, 164.70, 162.96, 161.01, 141.61, 137.35, 137.33, 134.26, 133.25, 131.20, 129.26, 129.19, 122.96, 121.36, 115.75, 115.58, 74.16, 51.87, 51.17, 45.78, 41.79, 39.45, 29.71, 29.25, 25.30, 14.14. **HRMS (ESI):** m/z calculated for $C_{27}H_{24}Br_2F2N_2O_2$, $[M+H]^+$ = 607.0230; found : 607.0204

4.4.1.3.11. 2-(4-(4-(2,5-dibromophenyl)-2-oxobutanoyl)piperazin-1-yl)benzonitrile (**BD19**)

White solid, 90 % yield. **^{1}H NMR (500 MHz, $CDCl_3$): δ** 7.60 (dd, *J* = 7.6, 1.7 Hz, 1H), 7.55 – 7.50 (m, 1H), 7.45 – 7.38 (m, 2H), 7.22 (dd, *J* = 8.4, 2.4 Hz, 1H), 7.09 (td, *J* = 7.6, 1.1 Hz, 1H), 7.01 (d, *J* = 8.2 Hz, 1H), 3.89 – 3.83 (m, 2H), 3.67 – 3.61 (m, 2H), 3.25 – 3.21 (m, 2H), 3.21 – 3.15 (m, 4H), 3.06 (t, *J* = 7.7 Hz, 2H). **^{13}C NMR (126 MHz, $CDCl_3$): δ** 199.17, 164.85, 154.93, 141.58, 134.35, 134.32, 133.99, 133.31, 131.27, 123.00, 122.98, 121.39, 119.15,

117.95, 107.00, 52.01, 51.33, 45.85, 41.90, 39.49, 31.94, 29.71, 29.37, 29.28, 22.70, 14.13. **HRMS (ESI):** m/z calculated for $C_{21}H_{19}Br_2N_3O_2$, $[M+H]^+$ = 505.9902; found : 505.9897

4.4.1.3.12. 1-(4-(benzo[d][1,3]dioxol-5-ylmethyl)piperazin-1-yl)-4-(4-(trifluoromethyl)phenyl)butane-1,2-dione (**BD20**)

Yellow liquid, 90 % yield. **^{1}H NMR (500 MHz, $CDCl_3$): δ** 7.54 (d, *J* = 8.1 Hz, 2H), 7.32 (d, *J* = 8.2 Hz, 2H), 6.82 (d, *J* = 1.7 Hz, 1H), 6.74 (d, *J* = 7.9 Hz, 1H), 6.72 – 6.68 (m, 1H), 5.95 (s, 2H), 3.60 (t, *J* = 5.2 Hz, 2H), 3.40 (s, 2H), 3.33 – 3.28 (m, 2H), 3.14 (t, *J* = 7.7 Hz, 2H), 3.03 (t, *J* = 7.3 Hz, 2H), 2.43 (t, *J* = 5.2 Hz, 2H), 2.32 (t, *J* = 5.1 Hz, 2H). **^{13}C NMR (126 MHz, CDCl3): δ** 199.58, 164.81, 147.78, 146.86, 144.32, 131.20, 128.74, 125.54, 125.51, 125.48, 122.22, 109.32, 107.96, 100.99, 62.46, 52.86, 52.19, 45.60, 41.67, 40.90, 28.68. **HRMS (ESI):** *m/z* calculated for $C_{23}H_{24}F_3N_2O_4$ $[M+H]^+$: 449.1688; found : 449.1644.

4.4.1.3.13. 1-(4-(bis(4-fluorophenyl)methyl)piperazin-1-yl)-4-(4-(trifluoromethyl)phenyl)butane-1,2-dione (**BD21**)

White solid, 90 % yield. **^{1}H NMR (500 MHz, $CDCl_3$): δ** 7.55 (d, *J* = 8.0 Hz, 2H), 7.38 – 7.31 (m, 6H), 7.04 – 6.97 (m, 4H), 4.25 (s, 1H), 3.70 – 3.55 (m, 2H), 3.33 (dd, *J* = 6.0, 4.2 Hz, 2H), 3.15 (t, *J* = 7.1 Hz, 2H), 3.03 (t, *J* = 7.3 Hz, 2H), 2.40 (t, *J* = 5.1 Hz, 2H), 2.28 (t, *J* = 5.0 Hz, 2H). **^{13}C NMR (126 MHz, CDCl3): δ** 199.49, 164.69, 162.96, 161.01, 144.29, 137.33, 137.30, 129.21, 129.15, 128.90, 128.73, 125.53, 125.50, 125.47, 125.44, 115.76, 115.59, 74.15, 60.42, 51.78, 51.13, 45.67, 41.75, 40.84, 28.71, 14.22. **HRMS (ESI):** *m/z* calculated for $C_{28}H_{26}F_5N_2O_2$ $[M+H]^+$: 517.1914; found : 517.1850

4.4.1.3.14. 1-(4-phenylpiperazin-1-yl)-4-(4-(trifluoromethyl)phenyl)butane-1,2-dione (**BD22**)

White solid, 90 % yield. **^{1}H NMR (500 MHz, $CDCl_3$): δ** 7.55 (d, *J* = 8.4 Hz, 2H), 7.35 (d, *J* = 8.2 Hz, 2H), 7.31 – 7.26 (m, 2H), 6.92 (dd, *J* = 13.7, 7.5 Hz, 3H), 3.77 (dd, *J* = 6.1, 4.4 Hz, 2H), 3.51 – 3.47 (m, 2H), 3.23 – 3.16 (m, 4H), 3.11 – 3.03 (m, 4H). **^{13}C NMR (126 MHz,**

$CDCl_3$): δ 199.40, 164.69, 150.69, 144.29, 129.33, 128.77, 128.70, 125.57, 125.54, 125.51, 125.48, 120.96, 116.91, 49.90, 49.45, 45.51, 41.69, 40.92, 28.71. **HRMS (ESI):** *m/z* calculated for $C_{21}H_{21}F_3N_2O_2$ $[M+H]^+$: 391.1633; found : 391.1596

4.4.1.3.15. 2-(4-(2-oxo-4-(4-(trifluoromethyl)phenyl)butanoyl)piperazin-1-yl)benzonitrile (**BD23**)

White solid, 95 % yield. **^{1}H NMR (500 MHz, $CDCl_3$)**: δ 7.59 (dtt, *J* = 23.0, 15.0, 8.5 Hz, 4H), 7.37 (dt, *J* = 26.7, 12.8 Hz, 2H), 7.14 (dt, *J* = 14.3, 7.5 Hz, 1H), 7.09 – 6.97 (m, 1H), 4.03 – 3.79 (m, 2H), 3.71 – 3.41 (m, 2H), 3.37 – 2.97 (m, 8H), 1.64 (d, *J* = 11.5 Hz, 2H). **^{13}C NMR (126 MHz, $CDCl_3$): δ** 199.38, 154.91, 144.29, 134.37, 134.01, 128.79, 128.75, 125.55, 123.05, 123.01, 119.14, 117.95, 106.98, 76.96, 76.78, 51.93, 51.36, 45.83, 41.93, 40.93, 28.74. **HRMS (ESI)**: *m/z* calculated for $C_{22}H_{20}F_3N_3O_2$ $[M+H]^+$: 416.1586; found : 416.1560. HPLC % Purity: 96.46

4.4.1.3.16. 1-(4-(2,5-dimethylphenyl)piperazin-1-yl)-4-(4-(trifluoromethyl)phenyl)butane-1,2-dione (**BD24**)

White solid, 90 % yield. **^{1}H NMR (500 MHz, $CDCl_3$): δ** 7.65 – 7.52 (m, 2H), 7.38 (d, *J* = 7.9 Hz, 2H), 7.28 (s, 1H), 7.10 (dd, *J* = 7.6, 2.0 Hz, 1H), 6.89 – 6.84 (m, 1H), 6.79 (d, *J* = 1.8 Hz, 1H), 3.77 (d, *J* = 5.0 Hz, 2H), 3.47 (dd, *J* = 6.8, 3.2 Hz, 2H), 3.21 (td, *J* = 7.2, 2.0 Hz, 2H), 3.09 (t, *J* = 7.3 Hz, 2H), 2.92 (q, *J* = 3.6, 2.0 Hz, 2H), 2.87 – 2.81 (m, 2H), 2.32 (d, *J* = 2.0 Hz, 3H), 2.27 (d, *J* = 2.0 Hz, 3H). **^{13}C NMR (126 MHz, $CDCl_3$): δ** 199.58, 165.03, 150.35, 144.33, 136.38, 131.04, 129.42, 128.78, 125.56, 125.53, 125.50, 124.67, 120.07, 51.98, 51.55, 46.20, 42.22, 40.97, 28.72, 21.13, 17.32. **HRMS (ESI):** *m/z* calculated for $C_{23}H_{25}F_3N_2O_2$ $[M+Na]^+$: 441.1766; found : 441.1746

4.4.1.3.17. 1-(4-(pyridin-2-yl)piperazin-1-yl)-4-(4-(trifluoromethyl)phenyl)butane-1,2-dione (**BD25**)

White solid, 90 % yield**. ^{1}H NMR (500 MHz, $CDCl_3$): δ** 8.22 (dd, *J* = 5.1, 1.9 Hz, 1H), 7.62 – 7.50 (m, 3H), 7.37 (d, *J* = 8.0 Hz, 2H), 6.71 (dd, *J* = 7.2, 4.9 Hz, 1H), 6.66 (d, *J* = 8.5 Hz, 1H), 3.75 (dd, *J* = 6.6, 4.0 Hz, 2H), 3.61 (dd, *J* = 6.6, 4.1 Hz, 2H), 3.53 (dd, *J* = 6.5, 3.2 Hz, 2H), 3.49 (dd, *J* = 6.4, 3.2 Hz, 2H), 3.22 (t, *J* = 7.3 Hz, 2H), 3.08 (t, *J* = 7.3 Hz, 2H). **^{13}C NMR (126 MHz, $CDCl_3$): δ** 199.35, 164.81, 158.82, 148.07, 144.29, 137.80, 128.95, 128.76, 125.57, 125.54, 125.51, 125.48, 125.27, 123.11, 114.28, 107.32, 45.54, 45.26, 44.97, 41.48, 40.91, 29.71, 28.70, 1.03**. HRMS (ESI):** *m/z* calculated for $C_{20}H_{21}F_3N_3O_2$ $[M+H]^+$: 392.1586; found : 392.1555

4.4.1.3.18. 1-(4-benzhydrylpiperazin-1-yl)-4-(4-(trifluoromethyl)phenyl)butane-1,2-dione (**BD26**)

White solid, 90 % yield. **^{1}H NMR (500 MHz, CDCl3): δ** 7.55 (d, J = 8.2 Hz, 2H), 7.42 (d, J = 5.3 Hz, 4H), 7.32 (q, J = 8.0 Hz, 6H), 7.22 (d, J = 5.8 Hz, 2H), 4.27 (s, 1H), 3.70 – 3.59 (m, 2H), 3.39 – 3.32 (m, 2H), 3.15 (t, J = 7.6 Hz, 2H), 3.04 (t, J = 7.3 Hz, 2H), 2.49 – 2.42 (m, 2H), 2.40 – 2.31 (m, 2H). **^{13}C NMR (126 MHz, CDCl3): δ** 199.56, 164.78, 144.34, 141.83, 128.73, 128.70, 127.83, 127.31, 125.54, 125.51, 125.48, 125.45, 75.82, 51.93, 51.27, 45.77, 41.82, 40.88, 29.73, 28.70. **HRMS (ESI):** *m/z* calculated for $C_{28}H_{27}F_3N_2O_2$ $[M+H]^+$: 481.2103; found : 481.2085

4.4.1.3.19. 1-(4-benzylpiperidin-1-yl)-4-(4-chlorophenyl)butane-1,2-dione (**BD27**)

White solid, 90 % yield. **^{1}H NMR (500 MHz, $CDCl_3$): δ** 7.35 – 7.20 (m, 6H), 7.20 – 7.11 (m, 3H), 4.47 (ddt, *J* = 13.3, 4.3, 2.3 Hz, 1H), 3.52 (ddt, *J* = 13.6, 4.6, 2.5 Hz, 1H), 3.18 – 3.01 (m, 2H), 2.97 (t, *J* = 7.3 Hz, 2H), 2.87 (ddd, *J* = 13.6, 12.5, 2.9 Hz, 1H), 2.61 (td, *J* = 12.9, 2.9 Hz, 1H), 2.58 – 2.50 (m, 2H), 1.78 (ddq, *J* = 16.1, 9.3, 3.2, 2.8 Hz, 2H), 1.66 – 1.62 (m, 1H), 0.89 (q, *J* = 11.2, 9.0 Hz, 1H). **^{13}C NMR (126 MHz, $CDCl_3$): δ** 200.28, 165.24, 139.64, 138.68, 132.12, 129.76, 129.07, 128.65, 128.38, 126.19, 45.90, 42.82, 41.87, 41.19, 38.14, 32.36, 31.48, 29.72, 28.23. **HRMS (ESI):** *m/z* calculated for $C_{22}H_{25}ClNO_2$ $[M+H]^+$: 370.1574; found

: 370.1550. HPLC % Purity: 98.02

4.4.1.3.20. 1-(4-benzylpiperidin-1-yl)-4-(2,5-dibromophenyl) butane-1,2-dione (**BD28**)

Yellow liquid, 78 % yield. **^{1}H NMR (500 MHz, $CDCl_3$): δ** 7.45 – 7.38 (m, 2H), 7.31 (td, *J* = 8.1, 7.6, 1.8 Hz, 4H), 7.27 – 7.21 (m, 2H), 7.21 – 7.12 (m, 2H), 4.49 (ddt, *J* = 13.2, 4.3, 2.3 Hz, 1H), 3.62 (ddt, *J* = 13.4, 4.6, 2.5 Hz, 1H), 3.19 – 3.10 (m, 1H), 3.10 – 3.03 (m, 2H), 3.00 – 2.90 (m, 1H), 2.69 – 2.52 (m, 3H), 1.87 – 1.73 (m, 2H), 1.69 (dt, *J* = 13.6, 3.1 Hz, 1H), 0.93 – 0.83 (m, 3H), 0.09 (s, 2H). **^{13}C NMR (126 MHz, $CDCl_3$): δ** 199.80, 139.64, 134.26, 133.31, 131.19, 129.08, 128.38, 126.19, 45.99, 42.83, 41.92, 39.45, 38.17, 32.45, 31.94, 31.50, 29.72, 29.23, 14.14. **HRMS (ESI):** *m/z* calculated for $C_{22}H_{23}Br_2NO_2$ $[M+H]^+$: 494.0153; found : 494.0122

4.4.2. In Vitro Assay

4.4.2.1. Aβ_{42} monomer preparation and ThT fluorescence assay

Recombinant amyloid-β peptide (Aβ42) was produced in BL21(DE3) *E. coli* cells with fused to a NT* solubility tag, and the fusion protein was purified by immobilized metal affinity chromatography (IMAC). Subsequently, the NT* solubility tag was enzymatically cleaved off using recombinant Tobacco Etch Virus (TEV) proteinase, and monomeric Aβ_{42} species were purified by immobilized metal affinity chromatography (IMAC) and size exclusion chromatography (SEC) as previously reported [17]. The concentration of monomeric Aβ_{42} was determined using an extinction coefficient of 1 424 M^{-1} cm^{-1} calculated based on absorbance at 280 nm and 300 nm.

For the analysis of Aβ_{42} fibrillization kinetics, a 20 µL solution containing 10 µmol L^{-1} Thioflavin T (ThT), 3 µmol L^{-1} Aβ_{42} monomer, and varying concentrations of different chemical compounds at different molar ratios relative to the Aβ_{42} monomer concentration, was added to each well of half-area 384-well microplates with clear bottoms (Corning Glass 3766, USA). The mixture (quadruplicates for each sample) was incubated at 37°C under quiescent conditions. ThT fluorescence was continuously recorded using a microplate reader (FLUOStar

Galaxy from BMG Labtech, Offenberg, Germany) with a 440 nm excitation filter and a 480 nm emission filter. All experiments were conducted using the same batch of $A\beta_{42}$ peptide, ensuring consistency and reliability in the obtained data. Each dataset was obtained from a single plate at the same time, maintaining experimental uniformity.

4.4.2.2. Analysis of $A\beta_{42}$ aggregation kinetics

To determine aggregation half time ($\tau_{1/2}$) and maximal growth rate (r_{max}), the fibrillization traces of the $A\beta_{42}$ peptide with varying concentrations of different small compounds were fitted to a sigmoidal equation given by Eq. (**1**) [18, 19] :

$$F = F_0 + A/(1 + exp[r_{max}\ (\tau_{1/2} - t)]\ ) \qquad \text{Eq. (1)}$$

Where *A* the amplitude and F_0 the base value.

The fibrillization traces of the total fibril mass concentration, denoted as *M(t)*, are described by the following integrated rate law [20]:

$$\frac{\boldsymbol{M(t)}}{\boldsymbol{M(\infty)}} = \mathbf{1} - \left(\frac{\boldsymbol{B_+ + C_+}}{\boldsymbol{B_+ + C_+(\kappa t)}} \cdot \frac{\boldsymbol{B_- + C_+ \cdot exp\ exp\ (\kappa t)}}{\boldsymbol{B_- + C_+}}\right)^{\frac{\boldsymbol{k_\infty^2}}{\boldsymbol{\kappa\, \tilde{k}_\infty}}} \cdot \qquad \text{Eq. (2)}$$

$$\boldsymbol{exp\ exp\ (-k_\infty t)}$$

Where the intermediate coefficients are functions of λ and κ. The parameters n_C and n_2 represent the reaction orders for primary and secondary nucleation, respectively:

$$C_\pm = \pm\, \lambda^2\ /2/\kappa^2$$

$$k_\infty = \sqrt{2\kappa^2/(n_2(n_2+1)) + 2\lambda^2/n_C}$$

$$\tilde{k}_\infty = \sqrt{k_\infty^2 - 4C_+C_-\kappa^2}$$

$$B_\pm = (k_\infty \pm \tilde{k}_\infty)/2/\kappa$$

$$\lambda = \sqrt{2 \cdot k_+ k_n \cdot m(0)^{n_C}}$$

$$\kappa = \sqrt{2 \cdot k_+ k_2 \cdot m(0)^{n_2+1}}$$

The microscopic rate constants k_n, k_+, and k_2 correspond to the rate constants for primary nucleation, elongation, and secondary nucleation, respectively. The fibrillization traces of $A\beta_{42}$ with and without the small compounds were fitted globally using the AmyloFit platform, employing a model where secondary nucleation dominates Eq. (**2**). In this model, either k_n, k_+ or k_2 serves as the sole fitting parameter. This approach allowed for a comprehensive analysis of the fibrillization process [21].

4.4.2.3. In vitro Heparin-Induced Tau Aggregation Assay

An aggregation buffer was prepared with a composition of 20 mM Tris (pH 7.4), 100 mM NaCl, and 1 mM EDTA. Once formulated, the buffer was stored at room temperature, where it remains stable for several months. Prior to its application, the buffer was supplemented with 1 mM dithiothreitol (DTT) [22]. Recombinant tau fragments, labeled SP-496 (Bio-Techne India Pvt Ltd) and weighing 100 µg, were dissolved in 100 µl of the 20 mM Tris reaction buffer, yielding a tau protein stock solution at a concentration of 20 µM. For experimental applications, a 15 µM tau protein solution was prepared using the aggregation buffer. Concurrently, a 1mM heparin stock solution was prepared, from which an 8 µM working solution was derived. Additionally, a 10 mM ThT stock solution was produced in the reaction buffer, and a 50µM ThT working solution was subsequently prepared for assay purposes. For the core experiment, tau protein was incubated for 72 hours at 37°C, either in the presence or absence of varying concentrations of compound BD23, in the reaction buffer (**Table 4.7**). The culmination of the incubation process involved the measurement of tau fibril content using ThT fluorescence, with an excitation wavelength of 450 nm and an emission wavelength of 485 nm, analyzed on a multi-mode plate reader [23].

Table 4.7. Tau protein aggregates preparation in the absence and presence of compound BD23.

Sample	Heparin (μM)	BD23 (μM)	Tau(μM)
Tau	0	0	15
Tau + Heparin	8	0	15
Tau+Heparin+ BD23	8	100	15
Tau+Heparin+ BD23	8	200	15

4.4.2.4. In Vitro Cytotoxicity Assay

Cytotoxicity assay was performed in a similar way as discussed in **Chapter 3, Section 3.4.7.2.** The SHSY5Y cell line was treated with 50 μM of the final concentration of the compound. Within the scope of this research, the SH-SY5Y cell line was utilized as it serves as an in vitro model for neuronal function and differentiation [24].

4.4.3. In Vivo Behavioral Studies of Compound BD23 in Aβ-induced Cognitive Deficit Mice Model.

4.4.3.1. Experimental animals: Swiss Albino Mice (25-40 gm) were used in the study. Animals were housed in five per cage in standard housing conditions; temperature 21 ± 2°C; 12-hour light-dark cycle. Animals were provided with standard laboratory food *ad-libitum* and sterile water. All the animals were randomly assigned to the different experimental groups (n=5/group). All experiments and methods used in this research followed the recommendations set by the Committee for the Control and Supervision of Animal Experiments, under the Ministry of Environment, Forests and Climate Change, India. We also received approval from the University's Central Animal Ethics Committee (IIT, BHU, Varanasi, India) with reference IAFC Approval Number: IIT(BHU)/IAEC/2012/005 and IIT(BHU)/IAEC/2012/006.

4.4.3.2. Drug Treatment

$A\beta_{25-35}$ (Biosynth Ltd) was dissolved in sterile distilled saline at a concentration of 5 nM, and

incubated at 37 °C for 4 days to obtain the aggregated form [25]. Under anesthesia, aggregates (5 nmol/ µl) were injected into the right ventricle, with stereotaxic coordinates from the bregma being, in mm, A -0.22, L -1.0, and V 2.5. All injections were carried out using a 10 µl Hamilton micro syringe. At 7 days after the i.c.v. injection of $A\beta_{25-35}$ aggregates, BD 23 (1,2 & 5 mg/kg, *i.p.*), and Donepezil (5 mg/kg, *i.p.*) were administered once daily for 14 days.

4.4.3.3. Learning and Memory Test

Memory acquisition and retention were tested using an elevated plus maze test [26]. The apparatus consisted of two crossed arms, one closed and the other, open. Each rat was placed on the open arm, facing outwards. The time taken by the rat to enter the closed arm in the first trial (acquisition trial) was noted and was called initial transfer latency. The cut-off time was fixed as 90 s and in case a rat could not find the closed arm within this period, it was gently pushed into one of the closed arms and allowed to explore the maze for 15 s. The second trial (retention trial) was performed 24 h after the acquisition trial and retention transfer latency was noted. The retention trial latency was expressed as a percentage of the initial trial latency.

4.4.3.4. Motor coordination

The rotarod test was performed as per previously published protocols with minor modifications [27]. Mice were placed in the testing room for at least 1hr before testing to minimize the effects of stress on behavior during testing. Animals from the same cage are placed in separate lanes on rod rotating at 5 rpm such that animals may walk forward to keep balance. After 60 s on the rod, animals are returned to their home cage. The procedure is repeated for a total of three trials separated by 10 min inter-trial intervals. The apparatus is set to accelerate from 4 to 40 rpm in 300 s, and animals from the same cage are placed in separate lanes on the rod initially rotating at 4 rpm. Trial begins when acceleration is started and ends when the animal falls off the rod. The procedure is repeated for a total of three trials separated by 15 min intertrial intervals.

4.4.3.5. Novel Object Recognition Test

The novel object recognition test was performed in a square open-field apparatus painted black in color [28]. Two identical objects (A, A') were placed at fixed distances within the square field. The mice were then placed at the center of the square field, and the number of contacts with each object. was recorded during a 10 min period (training session). The mice were placed back into the same field 24 h after the training session, and this time one of the objects was replaced with a new object (A, B). The mice were allowed to search freely for 10 min, and the number of contacts with the original and novel object was recorded (test session). Time spent with the novel object was calculated as a discrimination index (DI), defined as $(T_{new}-T_{old}) / T_{new} + T_{old})$.

4.4.4. Solubility Determination

Solubility is determined by preparing a concentrated stock solution (10 mM) in an organic solvent (usually DMSO), after which the 50 µL 10 mM DMSO stock was added to 950 µl of 1 M phosphate-buffered saline pH 7.4. Then the solution was allowed for 1.5 hr for mixing. The resultant solution was centrifuged, filtered using 0.2 µm nylon syringe filter and quantify by using the RP-HPLC method. Then quantified by using the RP-HPLC method. HPLC Instrument used: Agilent 2004, Method: Solvent system used = Acetonitrile: Water = 90:10. Column Specification: Poroshell 123, EC C18 4µm, 4.6*150mm [29].

4.4.5. PAMPA Assay

The BBB permeation is one of the most important parameters for all CNS-acting drugs. To treat neurological disorders, it is essential for all drugs to have good BBB permeability, even though this property also serves the purpose of protecting the brain from exposure to molecules that may be harmless to peripheral organs but toxic to neurons in the brain [30, 31]. So in order to check the BBB permeability of test compounds (BD23 and Donepezil) we performed a parallel artificial membrane permeability assay (PAMPA) by using PAMPA-BBB Kit [32, 33].

PAMPA-BBB Kit is purchased from BioAssay Systems along with all assemblies. BBB lipid solution 5 µl dissolved in dodecane was added directly to the membranes of the donor plate carefully in order to avoid the puncture of the membrane with a pipette tip. First 300 µL of PBS (pH 7.2) was added to wells in the acceptor plate. Then 200 µl of all 500 µm test compounds prepared in PBS (pH 7.2) and 500 µm of permeability control (positive and negative permeability control) were added to duplicate wells of the donor plate. The donor plate was placed carefully into the acceptor well and incubated at room temperature for 24 hours. After 24 hours the donor plate was carefully removed from acceptor plate and 100 µl acceptor solution was collected for each test and control along with blank control (PBS and DMDSO solution) were transferred to 96-well plate for analysis. The UV absorbance of all test and control compounds were taken by using multi-mode microplate reader (Spectramax M5) at 280 nm. The peak absorbance was determined for test compound and Permeability Control, Permeability Rate (Pe) was calculated by using the following calculation:

$$Pe = C \times \left(1 - \frac{OD_A}{OD_E}\right)\frac{cm}{s}$$

Where OD_A = absorbance of the Acceptor Solution Minus Blank, OD_E = absorbance of the equilibrium standard minus Blank, and, using an 24-hour incubation, C = 5.78×10^{-6}.

4.4.6. Computational Details

4.4.6.1. In silico Pharmacokinetic properties.

The pharmacokinetic attributes of the molecules were assessed in silico through the Swiss ADME webserver, accessible at http://www.swissadme.ch. The compound structures in SMILES were used for calculating the ADME parameters.

4.4.6.2. Molecular Docking

The molecular ducking study of all compounds was performed by using the Gnina tool [16]. Protein and ligand preparation were performed by using ADT, discussed in **Chapter 3**.

4.4.6.3. Molecular Dynamics

The molecular dynamic simulation of all the complexes was performed by using GROMACS 20.3 software. The parameters set for all complexes and methods for molecular dynamics simulation are well discussed in the **Chapter 3, Section 3.4.6**.

4.4.6.4. Quantum Chemical Calculations

The DFT study was performed as discussed in **Chapter 3, Section 3.4.5**.

4.5. Conclusion

In this chapter we have synthesized a total of twenty-eight compounds and characterized by NMR and HRMS techniques. All the synthesized compounds were evaluated for their efficacy against Aβ aggregation in vitro. Assays that were designed to assess amyloid aggregation in vitro disclosed that a significant number of these compounds were able to modulate Aβ, thereby delaying the aggregation process. Pharmacokinetic studies further elucidated the solubility of hits and permeability characteristics of compound BD23. Furthermore, activity assessments of BD23 against heparin-induced tau aggregation revealed that at a concentration of 100 μM, the compound inhibited the aggregation process. However, at 200 μM, no significant effect was observed. Cytotoxicity tests on SHSY5Y cell lines showed that all compounds were generally non-toxic, with the exception of compound BD11, which exhibited cytotoxic effects. Conversely, compound BD19 demonstrated a cell-proliferative effect. In vivo studies on Aβ-injected models indicated that the compound BD23 enhances cognitive activity at a dose of 5 mg/Kg. Additionally, molecular docking and dynamic studies provided insights into the binding interactions and the stability of the ligand when in the presence of Aβ and tau peptides. Quantum chemical calculations pertaining to BD23 also elucidated its electronic and thermal properties. In summary, the present study underscores the potential of BD23 as a promising lead compound for further research and development. The findings also advocate for a deeper

exploration of various heterocyclic derivatives of α-ketoamides as potential therapeutic agents against AD.

4.6. References

1. P. Scheltens, B. De Strooper, M. Kivipelto, H. Holstege, G. Chételat, C.E. Teunissen, J. Cummings, W.M. van der Flier, Alzheimer's disease, The Lancet, 397 (2021) 1577-1590.
2. M. Robello, E. Barresi, E. Baglini, S. Salerno, S. Taliani, F.D. Settimo, The alpha keto amide moiety as a privileged motif in medicinal chemistry: current insights and emerging opportunities, Journal of Medicinal Chemistry, 64 (2021) 3508-3545.
3. E. Popugaeva, D. Chernyuk, H. Zhang, T.Y. Postnikova, K. Pats, E. Fedorova, V. Poroikov, A.V. Zaitsev, I. Bezprozvanny, Derivatives of piperazines as potential therapeutic agents for Alzheimer’s disease, Molecular pharmacology, 95 (2019) 337-348.
4. P. Grover, S. Rohilla, M. Bhardwaj, L. Mehta, A. Malhotra, Piperidine Nucleus as a Promising Scaffold for Alzheimer’s Disease: Current Landscape and Future Perspective, Current Topics in Medicinal Chemistry, (2023).
5. A.R. Zala, P. Kumari, Versatile Therapeutic Values of N-Containing Heterocycles Benzimidazole, Piperazine and Piperidine Hybrids, ChemistrySelect, 8 (2023) e202301304.
6. P. Mishra, A. Kumar, G. Panda, Anti-cholinesterase hybrids as multi-target-directed ligands against Alzheimer’s disease (1998–2018), Bioorganic & Medicinal Chemistry, 27 (2019) 895-930.
7. D. Kumar, S.K. Gupta, A. Ganeshpurkar, G. Gutti, S. Krishnamurthy, G. Modi, S.K. Singh, Development of Piperazinediones as dual inhibitor for treatment of Alzheimer's disease, European journal of medicinal chemistry, 150 (2018) 87-101.
8. J.E. Mintzer, L.E. Tune, C.D. Breder, R. Swanink, R.N. Marcus, R.D. McQuade, A. Forbes, Aripiprazole for the treatment of psychoses in institutionalized patients with Alzheimer dementia: a multicenter, randomized, double-blind, placebo-controlled assessment of three fixed doses, The American Journal of Geriatric Psychiatry, 15 (2007) 918-931.
9. K. Mal, A. Sharma, P.R. Maulik, I. Das, PPh3· HBr-DMSO Mediated Expedient Synthesis of γ-Substituted β, γ-Unsaturated α-Ketomethylthioesters and α-Bromo

Enals: Application to the Synthesis of 2-Methylsulfanyl-3 (2 H)-furanones, Chemistry–A European Journal, 20 (2014) 662-667.

10. R. Maity, B. Das, I. Das, Transition-Metal-Free Reduction of α-Keto Thioesters with Hydrosilanes at Room Temperature: Divergent Synthesis through Reagent-Controlled Chemoselectivities, Advanced Synthesis & Catalysis, 361 (2019) 2347-2353.
11. B. Das, A.T. Baidya, A.T. Mathew, A.K. Yadav, R. Kumar, Structural modification aimed for improving solubility of lead compounds in early phase drug discovery, Bioorganic & Medicinal Chemistry, 56 (2022) 116614.
12. A.-R. Coltescu, M. Butnariu, I. Sarac, The importance of solubility for new drug molecules, Biomedical and Pharmacology Journal, 13 (2020) 577-583.
13. L.M. Lueptow, Novel object recognition test for the investigation of learning and memory in mice, JoVE (Journal of Visualized Experiments), (2017) e55718.
14. H. Shiotsuki, K. Yoshimi, Y. Shimo, M. Funayama, Y. Takamatsu, K. Ikeda, R. Takahashi, S. Kitazawa, N. Hattori, A rotarod test for evaluation of motor skill learning, Journal of neuroscience methods, 189 (2010) 180-185.
15. K. Zawadzińska, B. Gostyński, Nitrosubstituted analogs of isoxazolines and isoxazolidines: a surprising estimation of their biological activity via molecular docking, Scientiae Radices, 2 (2023) 25-46.
16. A.T. McNutt, P. Francoeur, R. Aggarwal, T. Masuda, R. Meli, M. Ragoza, J. Sunseri, D.R. Koes, GNINA 1.0: molecular docking with deep learning, Journal of cheminformatics, 13 (2021) 1-20.
17. X. Zhong, R. Kumar, Y. Wang, H. Biverstål, C. Ingeborg Jegerschöld, P. JB Koeck, J. Johansson, A. Abelein, G. Chen, Amyloid fibril formation of Arctic amyloid-β 1–42 peptide is efficiently inhibited by the BRICHOS domain, ACS Chemical Biology, 17 (2022) 2201-2211.
18. G. Chen, Y. Andrade-Talavera, S. Tambaro, A. Leppert, H.E. Nilsson, X. Zhong, M. Landreh, P. Nilsson, H. Hebert, H. Biverstål, Augmentation of Bri2 molecular chaperone activity against amyloid-β reduces neurotoxicity in mouse hippocampus in vitro, Communications Biology, 3 (2020) 32.
19. G. Chen, A. Abelein, H.E. Nilsson, A. Leppert, Y. Andrade-Talavera, S. Tambaro, L. Hemmingsson, F. Roshan, M. Landreh, H. Biverstål, Bri2 BRICHOS client specificity and chaperone activity are governed by assembly state, Nature Communications, 8 (2017) 2081.

20. S.I. Cohen, P. Arosio, J. Presto, F.R. Kurudenkandy, H. Biverstål, L. Dolfe, C. Dunning, X. Yang, B. Frohm, M. Vendruscolo, A molecular chaperone breaks the catalytic cycle that generates toxic Aβ oligomers, Nature structural & molecular biology, 22 (2015) 207-213.
21. G. Meisl, J.B. Kirkegaard, P. Arosio, T.C. Michaels, M. Vendruscolo, C.M. Dobson, S. Linse, T.P. Knowles, Molecular mechanisms of protein aggregation from global fitting of kinetic models, Nature protocols, 11 (2016) 252-272.
22. S. Alali, G. Riazi, M.R. Ashrafi-Kooshk, S. Meknatkhah, S. Ahmadian, M. Hooshyari Ardakani, B. Hosseinkhani, Cannabidiol inhibits tau aggregation in vitro, Cells, 10 (2021) 3521.
23. R. Crespo, W. Koudstaal, A. Apetri, In vitro assay for studying the aggregation of tau protein and drug screening, JoVE (Journal of Visualized Experiments), (2018) e58570.
24. A. Romero, E. Ramos, V. Castellano, M.A. Martínez, I. Ares, M. Martínez, M.R. Martínez-Larrañaga, A. Anadón, Cytotoxicity induced by deltamethrin and its metabolites in SH-SY5Y cells can be differentially prevented by selected antioxidants, Toxicology in Vitro, 26 (2012) 823-830.
25. C. Tohda, N. Matsumoto, K. Zou, M.R. Meselhy, K. Komatsu, Aβ (25–35)-induced memory impairment, axonal atrophy, and synaptic loss are ameliorated by M1, A metabolite of protopanaxadiol-type saponins, Neuropsychopharmacology, 29 (2004) 860-868.
26. J. Itoh, T. Nabeshima, T. Kameyama, Utility of an elevated plus-maze for dissociation of amnesic and behavioral effects of drugs in mice, European journal of pharmacology, 194 (1991) 71-76.
27. D.J. Joseph, M. Von Deimling, Y. Hasegawa, A.G. Cristancho, R.C. Ahrens-Nicklas, S.L. Rogers, R. Risbud, A.J. McCoy, E.D. Marsh, Postnatal Arx transcriptional activity regulates functional properties of PV interneurons, in: iScience, 2021, pp. 101999.
28. J.H. Kim, Q. Wang, J.M. Choi, S. Lee, E.J. Cho, Protective role of caffeic acid in an Aβ25-35-induced Alzheimer's disease model, Nutrition research and practice, 9 (2015) 480-488.
29. A. Wolf, S. Shimamura, F.B. Reinhard, Working with small molecules: Preparing and storing stock solutions and determination of kinetic solubility, Chemical Proteomics: Methods and Protocols, (2012) 265-271.

30. M. Adenot, R. Lahana, Blood-brain barrier permeation models: discriminating between potential CNS and non-CNS drugs including P-glycoprotein substrates, Journal of chemical information and computer sciences, 44 (2004) 239-248.
31. N.J. Abbott, Blood–brain barrier structure and function and the challenges for CNS drug delivery, Journal of inherited metabolic disease, 36 (2013) 437-449.
32. C. Nath, V.N. Badavath, A. Thakur, G. Ucar, O. Acevedo, M.U.M. Siddique, V. Jayaprakash, Curcumin-based pyrazoline analogues as selective inhibitors of human monoamine oxidase A, MedChemComm, 9 (2018) 1164-1171.
33. V. Piazzini, C. Rosseti, E. Bigagli, C. Luceri, A.R. Bilia, M.C. Bergonzi, Prediction of permeation and cellular transport of Silybum marianum extract formulated in a nanoemulsion by using PAMPA and Caco-2 cell models, Planta Medica, 83 (2017) 1184-1193.